

SPACECRAFT FORMATION CONTROL AND ESTIMATION VIA IMPROVED RELATIVE-MOTION DYNAMICS

David A. Cicci

**Auburn University
107 Samford Hall
Auburn, AL 36849-0001**

30 Mar 2017

Final Report

APPROVED FOR PUBLIC RELEASE; DISTRIBUTION IS UNLIMITED.



**AIR FORCE RESEARCH LABORATORY
Space Vehicles Directorate
3550 Aberdeen Ave SE
AIR FORCE MATERIEL COMMAND
KIRTLAND AIR FORCE BASE, NM 87117-5776**

DTIC COPY NOTICE AND SIGNATURE PAGE

Using Government drawings, specifications, or other data included in this document for any purpose other than Government procurement does not in any way obligate the U.S. Government. The fact that the Government formulated or supplied the drawings, specifications, or other data does not license the holder or any other person or corporation; or convey any rights or permission to manufacture, use, or sell any patented invention that may relate to them.

This report is the result of contracted fundamental research deemed exempt from public affairs security and policy review in accordance with SAF/AQR memorandum dated 10 Dec 08 and AFRL/CA policy clarification memorandum dated 16 Jan 09. This report is available to the general public, including foreign nationals. Copies may be obtained from the Defense Technical Information Center (DTIC) (<http://www.dtic.mil>).

AFRL-RV-PS-TR-2017-0052 HAS BEEN REVIEWED AND IS APPROVED FOR
PUBLICATION IN ACCORDANCE WITH ASSIGNED DISTRIBUTION STATEMENT.

//SIGNED//
THOMAS A. LOVELL
Program Manager

//SIGNED//
PAUL HAUSGEN, Ph.D.
Technical Advisor, Spacecraft Component Technology

//SIGNED//
JOHN BEAUCHEMIN
Chief Engineer, Spacecraft Technology Division
Space Vehicles Directorate

This report is published in the interest of scientific and technical information exchange, and its publication does not constitute the Government's approval or disapproval of its ideas or findings.

REPORT DOCUMENTATION PAGE			<i>Form Approved</i> <i>OMB No. 0704-0188</i>		
Public reporting burden for this collection of information is estimated to average 1 hour per response, including the time for reviewing instructions, searching existing data sources, gathering and maintaining the data needed, and completing and reviewing this collection of information. Send comments regarding this burden estimate or any other aspect of this collection of information, including suggestions for reducing this burden to Department of Defense, Washington Headquarters Services, Directorate for Information Operations and Reports (0704-0188), 1215 Jefferson Davis Highway, Suite 1204, Arlington, VA 22202-4302. Respondents should be aware that notwithstanding any other provision of law, no person shall be subject to any penalty for failing to comply with a collection of information if it does not display a currently valid OMB control number. PLEASE DO NOT RETURN YOUR FORM TO THE ABOVE ADDRESS.					
1. REPORT DATE (DD-MM-YYYY) 30-03-2017		2. REPORT TYPE Final Report		3. DATES COVERED (From - To) 18 Jul 2014 – 17 Mar 2017	
4. TITLE AND SUBTITLE Spacecraft Formation Control and Estimation Via Improved Relative-Motion Dynamics			5a. CONTRACT NUMBER FA9453-14-1-0235		
			5b. GRANT NUMBER		
			5c. PROGRAM ELEMENT NUMBER 62601F		
6. AUTHOR(S) David A. Cicci			5d. PROJECT NUMBER 8809		
			5e. TASK NUMBER PPM00019431		
			5f. WORK UNIT NUMBER EF123128		
7. PERFORMING ORGANIZATION NAME(S) AND ADDRESS(ES) Auburn University 107 Samford Hall Auburn, AL 36849-0001			8. PERFORMING ORGANIZATION REPORT NUMBER		
9. SPONSORING / MONITORING AGENCY NAME(S) AND ADDRESS(ES) Air Force Research Laboratory Space Vehicles Directorate 3550 Aberdeen Ave, SE Kirtland AFB, NM 87117-5776			10. SPONSOR/MONITOR'S ACRONYM(S) AFRL/RVSV		
			11. SPONSOR/MONITOR'S REPORT NUMBER(S) AFRL-RV-PS-TR-2017-0052		
12. DISTRIBUTION / AVAILABILITY STATEMENT Approved for public release; distribution is unlimited.					
13. SUPPLEMENTARY NOTES					
14. ABSTRACT This research focused on improved spacecraft relative dynamics modeling and analysis, estimation of spacecraft relative motion, and control of spacecraft relative motion, with particular emphasis on estimation (i.e. navigation) of spacecraft relative trajectories from angles-only data.					
15. SUBJECT TERMS Orbital Mechanics; Satellite Formation Flying; Satellite Rendezvous; Satellite Proximity Operations					
16. SECURITY CLASSIFICATION OF:			17. LIMITATION OF ABSTRACT Unlimited	18. NUMBER OF PAGES 72	19a. NAME OF RESPONSIBLE PERSON Thomas A. Lovell
a. REPORT Unclassified	b. ABSTRACT Unclassified	c. THIS PAGE Unclassified			19b. TELEPHONE NUMBER (include area code)

(This page intentionally left blank)

TABLE OF CONTENTS

Section	Page
List of Figures	iii
List of Tables	iv
Preface	v
Acknowledgement and Disclaimer	vi
1 Summary	1
2 Introduction	2
3 Methods, Assumptions, and Procedures	9
3.1 Basic Description of IROD Approach	9
3.1.1 Guaranteed Ambiguity (“Woffinden’s Dilemma”)	9
3.1.2 Utilization of Nonlinear Dynamics	11
3.1.3 Utilization of Nonhomogeneous Dynamics	12
3.2 Detailed Description of IROD Algorithms	15
3.2.1 Linear Matrix Method (LMM)	15
3.2.2 Matrix Resultant Method (MRM)	20
3.2.3 Nonhomogeneous Observer Method (NOM)	22
3.2.4 Practical Considerations	23
3.3 Description of Scenarios	23
3.3.1 Ground-Based IROD (GIROD)	24
3.3.2 Close-Proximity IROD (CIROD)	25
3.3.3 Delineation of IROD test cases	25
3.4 Data Requirements for Scenarios, with Description of Data Flow	27
3.4.1 GIROD	27
3.4.2 CIROD	29
3.4.3 Output Metrics and Verification	33
3.4.4 Relative Orbit Elements	33
4 Results and Discussion	36
4.1 GIROD	36
4.1.1 GIROD Scenario 1	36
4.1.2 GIROD Scenario 2	38
4.1.3 GIROD Scenario 3	39
4.1.4 Assessment of GIROD Results	39
4.2 CIROD	40
4.2.1 CIROD Scenario 1	40
4.2.2 CIROD Scenario 2	42
4.2.3 CIROD Scenario 3	44
4.2.4 CIROD Scenario 4	45
4.2.5 CIROD Scenario 5	46

4.2.6	CIROD Scenario 6	49
4.2.7	CIROD Scenario 7	51
4.2.8	CIROD Scenario 8	53
5	Conclusions.....	56
6	Recommendations.....	58
	References.....	59
	List of Symbols, Abbreviations, and Acronyms	61

LIST OF FIGURES

Figure	Page
Figure 1. LVLH Coordinate Frame, with X and Y Axis Directions Depicted and Z Going into the page.....	2
Figure 2. Various “Families” of Ambiguous Trajectories (all 5 Assumptions in Force)	10
Figure 3. Notional Depiction of Two Trajectories Propagated with Nonlinear Dynamics	12
Figure 4. Notional Depiction of LOS Measurements Taken by Maneuvering Observer.....	15
Figure 5. Flow Chart of Ground-based IROD Algorithmic Process.....	28
Figure 6. Flow Chart of Close-proximity IROD Algorithmic Process	30
Figure 7. GIROD Scenario 1, with Observed Lines of Sight From Ground Sensor, Superimposed with True Propagated Trajectory (Blue) and IROD Solution Trajectory (Green)	37
Figure 8. LVLH Trajectory of IROD Solution for CIROD Scenario 1 (x vs. y), with LOS Measurements and True Relative Orbit Displayed.....	41
Figure 9. LVLH Trajectory of IROD Solution for CIROD Scenario 1 (z vs. t), with True Relative Orbit Displayed.....	42
Figure 10. LVLH Trajectory of IROD Solution for CIROD Scenario 2 (x vs. y), with LOS Measurements and True Relative Orbit Displayed	43
Figure 11. LVLH Trajectory of IROD Solution for CIROD Scenario 2 (z vs. t), with True Relative Orbit Displayed	44
Figure 12. LVLH Trajectory of IROD Solution for CIROD Scenario 3 (x vs. y), with LOS Measurements and True Relative Orbit Displayed	45
Figure 13. LVLH Trajectory of IROD Solution for CIROD Scenario 4 (x vs. y), with LOS Measurements and True Relative Orbit Displayed	46
Figure 14. LVLH Trajectory of IROD Solution for CIROD Scenario 5 (x vs. y), with LOS Measurements and True Relative Orbit Displayed	48
Figure 15. LVLH Trajectory of IROD Solution for CIROD Scenario 5 (z vs. t), with True Relative Orbit Displayed.....	48
Figure 16. LVLH Trajectory of IROD Solution for CIROD Scenario 6 (x vs. y), with LOS Measurements and True Relative Orbit Displayed	50
Figure 17. LVLH Trajectory of IROD Solution for CIROD Scenario 6 (z vs. t), with True Relative Orbit Displayed.....	50
Figure 18. LVLH Trajectory of IROD Solution for CIROD Scenario 7 (x vs. y), with LOS Measurements and True Relative Orbit Displayed	52
Figure 19. LVLH Trajectory of IROD Solution for CIROD Scenario 7 (z vs. t), with True Relative Orbit Displayed.....	53
Figure 20. LVLH Trajectory of IROD Solution for CIROD Scenario 8 (x vs. y), with LOS Measurements and True Relative Orbit Displayed	54
Figure 21. LVLH Trajectory of IROD Solution for CIROD Scenario 8 (z vs. t), with True Relative Orbit Displayed.....	55

LIST OF TABLES

Table	Page
Table 1. The Three Possible Delineations of Test Case Parameters in the Experiments to Follow...	26
Table 2. Description of GIROD Scenario 1, Including Table 1 Parameter Values	36
Table 3. Orbital Elements from Scenario 2 for (a) Constructed Reference Orbit, (b) First IROD Solution, (c) Second IROD Solution, (d) True Orbit	38
Table 4. Description of GIROD Scenario 2, Including Table 1 Parameter Values	38
Table 5. Orbital Elements from Scenario 2.....	38
Table 6. Description of GIROD Scenario 3, Including Table 1 Parameter Values	39
Table 7. Orbital Elements from Scenario 3.....	39
Table 8. Description of CIROD Scenario 1, including Table 1 parameter values	40
Table 9. True Relative Orbit of CIROD Scenarios 1-4, in Terms of ROE Values	40
Table 10. RMS Residual Angle Error and ROE Ratios for CIROD Scenarios 1-8	41
Table 11. Description of CIROD Scenario 2, Including Table 1 Parameter Values.....	42
Table 12. Description of CIROD Scenario 3, Including Table 1 Parameter Values	44
Table 13. Description of CIROD Scenario 4, Including Table 1 Parameter Values	45
Table 14. Description of CIROD Scenario 5, Including Table 1 Parameter Values	46
Table 15. True Relative Orbit of CIROD Scenarios 5-6, in Terms of ROE Values	46
Table 16. RMS Residual Angle Error and ROE Ratios/Differences for CIROD Scenarios 5-6.....	47
Table 17. Description of CIROD Scenario 6, Including Table 1 Parameter Values	49
Table 18. Description of CIROD Scenario 7, Including Table 1 Parameter Values	51
Table 19. True Relative Orbit of CIROD Scenarios 7-8 (Pre-maneuver), in Terms of ROE Values.....	51
Table 20. RMS Residual Angle Error and ROE Ratios/differences for CIROD Scenarios 7-8	52
Table 21. Description of CIROD Scenario 8, Including Table 1 Parameter Values	53

PREFACE

This final report represents the work conducted under Contract FA9453-14-1-0235 from 07/18/2014 to 10/15/2016. This project was directed by Principal Investigators (PI) Dr. David A. Cicci of Auburn University. The PI was assisted by graduate student Ms. Laura Hebert. The particular emphasis is on estimation of relative motion, detailing the development and test of algorithms collectively termed initial relative orbit determination.

ACKNOWLEDGEMENT

This material is based on research sponsored by Air Force Research Laboratory under agreement number FA9453-14-1-0235. The U.S. Government is authorized to reproduce and distribute reprints for Governmental purposes notwithstanding any copyright notation thereon.

DISCLAIMER

The views and conclusions contained herein are those of the authors and should not be interpreted as necessarily representing the official policies or endorsements, either expressed or implied, of Air Force Research Laboratory or the U.S. Government.

1 SUMMARY

Spacecraft inertial navigation, or the means by which an active spacecraft determines its ephemeris, is the foundation for most space missions [1]. For inactive or non-cooperative space objects, the same task can be performed, but in this case it must be done by passive means, and is often termed orbit determination [2]. These tasks, based on the physics of inertial orbital motion, each have an analog in the realm of relative orbital motion. In the case of navigation, a spacecraft can estimate its ephemeris (or improve its current estimate of its ephemeris) based on measurements between itself and a reference object whose orbit is accurately known [3-5]. In the case of orbit determination, a spacecraft whose own orbit is accurately known can estimate the ephemeris of an unknown object based on measurements between itself and that object [6-7]. Mathematically, these two tasks are essentially the same; in both cases, measurements between the spacecraft and a Resident Space Object (RSO) are processed to estimate the relative trajectory between the two objects. This research effort analyzes the processing of optical (angle or line-of-sight) sensor data from an active spacecraft to estimate just such a relative trajectory. Various mission scenarios are investigated, to include both close-proximity scenarios (when the spacecraft images a nearby RSO) and long-range scenarios (when the spacecraft images other RSOs). The methods detailed herein are meant to generate an initial guess of the relative orbit and can be considered deterministic in nature; i.e. the methods assume no modeling error (the relative dynamics on which the methods are based are assumed exact) and no measurement error (the measurements obtained are assumed exact). Therefore, the general term to be used for these methods is Initial Relative Orbit Determination (IROD). The IROD solution can serve as an initial guess or starter solution for a statistical (e.g. batch least-squares or Extended Kalman Filter) estimator. In addition, the IROD approach can be applied to classical (ground-based) tracking. Scenarios involving ground sensor data of either the spacecraft or the RSO will be explored. This document contains the following sections: a general description of IROD theory is given, followed by a detailed description of the various IROD techniques developed (with an input-output description of the data flow), delineation of each scenario, results, and conclusions.

2 INTRODUCTION

It is well-known that when trying to determine an object's orbit using strictly optical measurements ("angles-only"), observability can be an issue. Generally speaking, an orbit determination scenario is observable if the object's orbit can be uniquely determined from the given measurements. Unobservability implies ambiguity, i.e. there exist more than one orbit that fit the given measurements. This is most easily demonstrated in a relative orbit determination scenario [8], where both the observer and RSO are orbiting the Earth. Suppose we model the relative motion between the observer and RSO in a Cartesian coordinate frame. The logical frame then to employ is the Local-vertical-local-horizontal (LVLH) frame. This frame entails defining a reference orbit about the Earth, defining a "chief" object on this orbit, and attaching a coordinate frame to the chief's center of mass. This is depicted in Figure 1. Note that the LVLH frame is not predicated on the existence of two space objects, or even one for that matter, as the chief and its orbit can be fabricated. The frame is also not predicated on the chief orbit having any particular eccentricity (though for most practical applications, this orbit should be closed, i.e. $e < 1$). The LVLH coordinate directions are then defined as follows: the "x" or radial direction is aligned with the chief's inertial position vector (i.e. the vector from Earth's center to the chief), the "z" or cross-track direction is aligned with the chief's angular momentum vector (i.e. perpendicular to the chief's orbit plane), and the "y" direction is the cross product of z and x. (If the chief orbit is circular, the "y" direction is then aligned with the chief's inertial velocity vector and is often called along-track.) Note that the LVLH frame translates and rotates around the Earth with the chief object, therefore these directions are defined instantaneously.

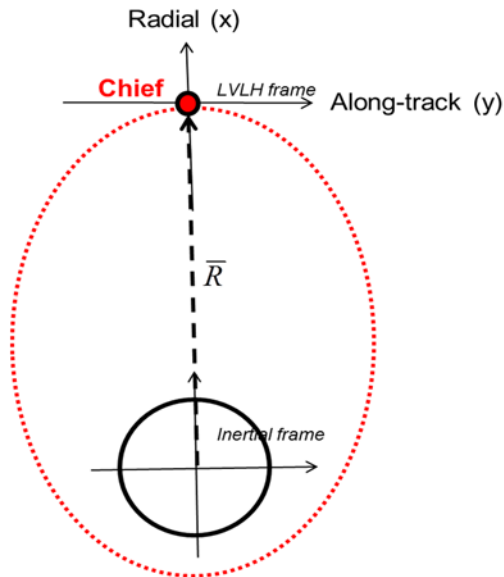


Figure 1. LVLH Coordinate Frame, with X and Y Axis Directions Depicted and Z Going into the page.

Note on Figure 1: Orbital Motion is Clockwise and \bar{R} Denotes Chief's Inertial Position Vector

If we choose the observer to be the chief, then the state vector $\bar{x}(t)$ consists of the relative position and velocity of the RSO expressed in LVLH coordinates: $\bar{x} = [x \ y \ z \ \dot{x} \ \dot{y} \ \dot{z}]^T$. Suppose the motion of the RSO relative to the reference orbit is described by linear dynamics, i.e.

$$\bar{x}(t) = \Phi(t_0, t) \bar{x}_0 \quad (1)$$

where $\bar{x}(t)$ represents the values of the states at any time t , \bar{x}_0 is a 6x1 vector represents the values of the states at the initial time t_0 , and $\Phi(t, t_0)$ is the 6 x 6 state transition matrix representing the linear dynamics of the motion. Two common choices for the state transition matrix are that derived from the Tschauner-Hempel solution [11] or that derived from the Clohessy-Wiltshire solution [12]. Both solutions assume the space objects are subject only to two-body (Keplerian) gravity force, with the Clohessy-Wiltshire solution containing the added assumption that the chief's orbit is circular.

Let us represent $\bar{x}(t)$ as

$$\bar{x}(t) = \begin{bmatrix} \bar{r}(t) \\ \bar{v}(t) \end{bmatrix} \quad (2)$$

The instantaneous Line-of-sight (LOS) from observer to RSO is the unit vector along the relative position vector:

$$\hat{u}_r(t) = \frac{\bar{r}(t)}{|\bar{r}(t)|} \quad (3)$$

The instantaneous relative position vector is related to the relative position vector at t_0 by

$$\bar{r}(t) = [\Phi_{rr}(t, t_0) \quad \Phi_{rv}(t, t_0)] \bar{x}_0 \quad (4)$$

where $\Phi_{rr}(t_0, t)$ and $\Phi_{rv}(t_0, t)$ are the upper left and upper right submatrices of $\Phi(t_0, t)$, respectively. Inserting Equation (4) into Equation (3) yields

$$\hat{u}_r(t) = \frac{[\Phi_{rr}(t, t_0) \quad \Phi_{rv}(t, t_0)] \bar{x}_0}{|[\Phi_{rr}(t, t_0) \quad \Phi_{rv}(t, t_0)] \bar{x}_0|} \quad (5)$$

Consider two trajectories, one whose values at t_0 are given by \bar{x}_{01} and the other whose initial values are $\bar{x}_{02} = \alpha \bar{x}_{01}$, where α is a positive real number. At any given time t , the line-of-sight vector to an RSO on the first trajectory is

$$\hat{u}_{r1}(t) = \frac{[\Phi_{rr}(t, t_0) \quad \Phi_{rv}(t, t_0)] \bar{x}_{01}}{|[\Phi_{rr}(t, t_0) \quad \Phi_{rv}(t, t_0)] \bar{x}_{01}|} \quad (6)$$

while the line-of-sight vector to an RSO on the second trajectory is

$$\begin{aligned} \hat{u}_{r2}(t) &= \frac{[\Phi_{rr}(t, t_0) \quad \Phi_{rv}(t, t_0)] \bar{x}_{02}}{|[\Phi_{rr}(t, t_0) \quad \Phi_{rv}(t, t_0)] \bar{x}_{02}|} = \frac{[\Phi_{rr}(t, t_0) \quad \Phi_{rv}(t, t_0)] \alpha \bar{x}_{01}}{|[\Phi_{rr}(t, t_0) \quad \Phi_{rv}(t, t_0)] \alpha \bar{x}_{01}|} \\ &= \frac{[\Phi_{rr}(t, t_0) \quad \Phi_{rv}(t, t_0)] \bar{x}_{01}}{|[\Phi_{rr}(t, t_0) \quad \Phi_{rv}(t, t_0)] \bar{x}_{01}|} = \hat{u}_{r1}(t) \end{aligned} \quad (7)$$

Because time t is arbitrary, clearly the two trajectories possess the same line-of-sight history for all time. Thus, for a trajectory initially at \bar{x}_0 , any trajectory $\alpha \bar{x}_0$ will possess the same line-of-sight history. Thus, a given line-of-sight history represents an infinite “family” of ambiguous trajectories.

It is important to understand exactly what assumptions lead to the above ambiguity. Reference 8 lists the following assumptions to guarantee such ambiguity:

- 1) Linear dynamics used to model the relative motion between the objects
- 2) Angle/LOS measurements only
- 3) No maneuvers by either object

However, these assumptions do not fully convey the requirements (or constraints) on the mission scenario that will guarantee ambiguity. The analysis below reveals a more accurate set of assumptions that will result in the ambiguity described above. Consider the fact that each LOS measurement above only contains two independent pieces of information, which can be expressed as angles (e.g. azimuth/elevation (Az/EI) or right ascension/declination (RA/Dec)) or slopes. Expressing the measurements as slopes, we have at each measurement time t_i :

$$\beta_i = \frac{u_y(t_i)}{u_x(t_i)}, \quad \gamma_i = \frac{u_z(t_i)}{u_x(t_i)} \quad (8)$$

Noting that $u_x(t_i) = \frac{x(t_i)}{\|\bar{r}(t_i)\|}$, $u_y(t_i) = \frac{y(t_i)}{\|\bar{r}(t_i)\|}$, and $u_z(t_i) = \frac{z(t_i)}{\|\bar{r}(t_i)\|}$, we have

$$\beta_i = \frac{y(t_i)}{x(t_i)}, \quad \gamma_i = \frac{z(t_i)}{x(t_i)} \quad (9)$$

Substituting for $x(t)$, $y(t)$, and $z(t)$ using Equation 1 yields

$$\beta_i = \frac{\Phi_2(t_i, t_0)\bar{x}_0}{\Phi_1(t_i, t_0)\bar{x}_0}, \quad \gamma_i = \frac{\Phi_3(t_i, t_0)\bar{x}_0}{\Phi_1(t_i, t_0)\bar{x}_0} \quad (10)$$

where $\Phi_1(t_0, t_i)$ is the first row of the state transition matrix, etc. We can rearrange each β and γ measurement equation as

$$\Phi_2(t_i, t_0)\bar{x}_0 - \beta_i \Phi_1(t_i, t_0)\bar{x}_0 = 0, \quad \Phi_3(t_i, t_0)\bar{x}_0 - \gamma_i \Phi_1(t_i, t_0)\bar{x}_0 = 0 \quad (11)$$

or

$$[\Phi_2(t_i, t_0) - \beta_i \Phi_1(t_i, t_0)]\bar{x}_0 = 0, \quad [\Phi_3(t_i, t_0) - \gamma_i \Phi_1(t_i, t_0)]\bar{x}_0 = 0 \quad (12)$$

Suppose we obtain LOS measurements at p different times, collecting $2p$ total pieces of information $(\beta_1, \beta_2, \dots, \beta_n, \gamma_1, \gamma_2, \dots, \gamma_n)$. Our $2p$ measurement equations are then

$$\begin{aligned}
[\Phi_2(t_1, t_0) - \beta_1 \Phi_1(t_1, t_0)] \bar{x}_0 &= 0 \\
[\Phi_3(t_1, t_0) - \gamma_1 \Phi_1(t_1, t_0)] \bar{x}_0 &= 0 \\
[\Phi_2(t_2, t_0) - \beta_2 \Phi_1(t_2, t_0)] \bar{x}_0 &= 0 \\
[\Phi_3(t_2, t_0) - \gamma_2 \Phi_1(t_2, t_0)] \bar{x}_0 &= 0 \\
\circ & \\
\circ & \\
\circ & \\
[\Phi_2(t_n, t_0) - \beta_n \Phi_1(t_n, t_0)] \bar{x}_0 &= 0 \\
[\Phi_3(t_n, t_0) - \gamma_n \Phi_1(t_n, t_0)] \bar{x}_0 &= 0
\end{aligned} \tag{13}$$

These equations can be written as $A\bar{x}_0 = 0$, where A is a $2p \times 6$ matrix whose elements are all constants, functions of the observer's orbit, or functions of the measurement times (therefore all elements of A are known). It is well known from linear algebra that if A is full rank, the only solution is the zero vector. Physically, this corresponds to a situation where there is no trajectory under the assumed dynamics that exactly satisfies the constraints of the given measurements (i.e. that possesses that particular LOS history). If A is less than full rank (i.e. singular), there is one nonzero solution for each degree of the null space of A . However, these nonzero solutions are non-unique, i.e. if \bar{x}_0^* is a solution, so is $\alpha \bar{x}_0^*$, where α is any real constant. This verifies the guaranteed ambiguity shown in Equation (7) above. Inspection of the above derivation shows that *ambiguity is guaranteed if the measurement equations are linear and homogeneous in the initial states*. This sufficiency condition is arguably the most fundamental way to explain the ambiguity detailed above. For reasons that will be seen later, it is useful to decompose this condition into the following two conditions that equivalently guarantee ambiguity:

- 1) The relative motion between the objects are described by linear homogeneous dynamics (i.e. the relative states at any time can be expressed entirely as linear combinations of the initial relative states).
- 2) The relationships between the measurements and states at each measurement time are linear and homogeneous (i.e. these relationships can be written as homogeneous equations that are linear in the instantaneous relative states).

These two assumptions quite evidently lead to the result in Equation (7). Again, for reasons that will be seen below, these assumptions can be further decomposed into the following:

- 1a) The relative motion between the objects are described by linear dynamics.

- 1b) No external (non-homogenous) forces act on the objects. This includes maneuvers, non-conservative forces, and rigid-body contact forces such as those exerted on a camera that is separated from the observer's center of mass.
- 1c) Measurements are taken by a single observer.
- 2a) Angle/LOS measurements only
- 2b) The relative motion is modeled in a Cartesian coordinate frame.

Note that, while these assumptions are equivalent to the single assumption originally stated above, they may not be unique; i.e. even if not all five of these assumptions are met, it may still be possible to guarantee the ambiguity of Equation (7) by formulating a different set of assumptions that are also equivalent to the original assumption. However, for the scenarios detailed in this report, this particular set of assumptions will serve as the chosen set to guarantee ambiguity.

Herein lies the crux of these scenarios. Given that ambiguity is guaranteed if all 5 total assumptions are met, it stands to reason that relaxing any one or more of these restrictions (i.e. “violating” one or more of the assumptions) may potentially yield observability, i.e. a unique relative state solution. Examples of such “relaxations” include the following:

- Use of nonlinear dynamics to describe the relative motion between the objects (relaxation of Assumption 1a)
- Executing (and accounting for) one or more known maneuvers by either the observer or RSO (relaxation of Assumption 1b)
- Accounting for non-conservative forces (e.g. drag or Solar Radiation Pressure) (SRP) in the relative motion dynamics (relaxation of Assumption 1b)
- Installing the camera a certain distance apart from the observer’s center of mass (relaxation of Assumption 1b)
- Processing other measurement types besides Angles/LOS (relaxation of Assumption 2a)
- Modeling the relative motion in a curvilinear (cylindrical or spherical) coordinate frame (relaxation of Assumption 2b)
- Processing measurements by multiple observers (relaxation of Assumption 1c)

Note that these “relaxations” are mutually exclusive, e.g. one may account for non-conservative forces within a *linear* relative motion model and still have a hope of observability. For these scenarios, IROD algorithms are devised based only on the first two “relaxations” listed above. These algorithms are tested on simulated optical measurement data. A variety of different accuracy metrics are employed. A major part of this investigation is to evaluate how well each “relaxation” adds to the observability and accuracy of angles-only IROD in various mission scenarios.

Before proceeding, the motivation for a relative dynamics approach to initial orbit determination (as opposed to an inertial dynamics approach, or “classical” Initial Orbit Determination (IOD)) should be pointed out. One advantage of a relative approach is that several closed-form (explicit) relative motion solutions exist. These solutions provide excellent insight into the motion, easy visualization, etc, and allow the possibility of closed-form IROD algorithms, i.e. algorithms that are non-iterative in nature. Such algorithms have been developed and are detailed in the sections that follow. These algorithms do not require any specific knowledge of the RSO (other than the LOS measurements themselves) in order to determine its relative orbit. The algorithms are attractive for autonomous/on-board implementation (or ground implementation during the hectic pace of mission operations) because they do not require human-in-the-loop supervision. Compare this to classical IOD schemes [9-10], which tend to be iterative in nature.

3 METHODS, ASSUMPTIONS, AND PROCEDURES

3.1 Basic Description of IROD Approach

In this section, the condition of guaranteed ambiguity (all assumptions in force) will be further described, then the effect of the first two “relaxations” in the bulleted list above will be described and how each of these “relaxations” leads to a candidate IROD algorithm.

3.1.1 Guaranteed Ambiguity (“Woffinden’s Dilemma”)

For the scenario of guaranteed ambiguity in Section 1, as governed by Equation’s (1)-(7), all five assumptions listed above are in force. In order to illustrate the nature of the IROD algorithms that follow, here we derive the measurement equations a slightly different way than in Section 1. Consider a measured LOS vector at time t_i in the LVLH frame, i.e. $\hat{u}_r(t_i) = u_x(t_i)\hat{i} + u_y(t_i)\hat{j} + u_z(t_i)\hat{k}$. The measurement equations can be formed by requiring that the relative position vector is parallel to each measured LOS:

$$\hat{u}_r(t_i) \times \bar{r}(t_i) = U(t_i)\bar{r}(t_i) = \begin{bmatrix} 0 & -u_z(t_i) & u_y(t_i) \\ u_z(t_i) & 0 & -u_x(t_i) \\ -u_y(t_i) & u_x(t_i) & 0 \end{bmatrix} \bar{r}(t_i) = 0 \quad (14)$$

or

$$\begin{aligned} u_z(t_i)y(t_i) - u_y(t_i)z(t_i) &= 0 \\ u_z(t_i)x(t_i) - u_x(t_i)z(t_i) &= 0 \\ u_y(t_i)x(t_i) - u_x(t_i)y(t_i) &= 0 \end{aligned} \quad (15)$$

Note that only two of the three above equations are independent, but we may include all three equations without loss of generality. Further, the state-transition matrix can be used to relate the relative position vector to the initial state vector:

$$\begin{bmatrix} 0 & -u_z(t_i) & u_y(t_i) \\ u_z(t_i) & 0 & -u_x(t_i) \\ -u_y(t_i) & u_x(t_i) & 0 \end{bmatrix} [\Phi_{rr}(t_i, t_0) \quad \Phi_{rv}(t_i, t_0)] \bar{\mathbf{x}}_0 = 0 \quad (16)$$

So if we obtain LOS measurements at n different times, the measurement equations can be written as $A\bar{\mathbf{x}}_0 = 0$, as in Section 1. Once again, if there exists a nonzero solution $\bar{\mathbf{x}}_0^*$, then any $\alpha\bar{\mathbf{x}}_0^*$ is a solution as well. Thus, a “direction” state vector can be determined that satisfies the measurement equations (denote this as $\tilde{\mathbf{x}}_0$ —a non-unique solution), but the magnitude of the state vector (denote this as α) cannot be determined. This is often referred to as “range ambiguity” and is depicted in Figure 2 (where the Clohessy-Wiltshire solution is used to propagate the relative motion). Each plot shows multiple trajectories sharing the same $\tilde{\mathbf{x}}_0$ but each with a different α . Note that the trajectories shown include some that might be considered “common” or “practical” for a proximity operations mission, as well as more obscure trajectories. The point is that the relative state vector may consist of any six real values (representing an infinite space of $\tilde{\mathbf{x}}_0$ in \mathcal{R}^6), and for any given $\tilde{\mathbf{x}}_0$, α can take on any positive real value (representing an infinite “family” of ambiguous trajectories for that $\tilde{\mathbf{x}}_0$). This scenario of guaranteed ambiguity will be referred to as “Woffinden’s Dilemma” because it was first described in Reference 8. Note that this guaranteed ambiguity is not a function of how many measurements are taken; i.e. if all the assumptions guaranteeing ambiguity are in force, one cannot somehow create observability by taking more measurements.

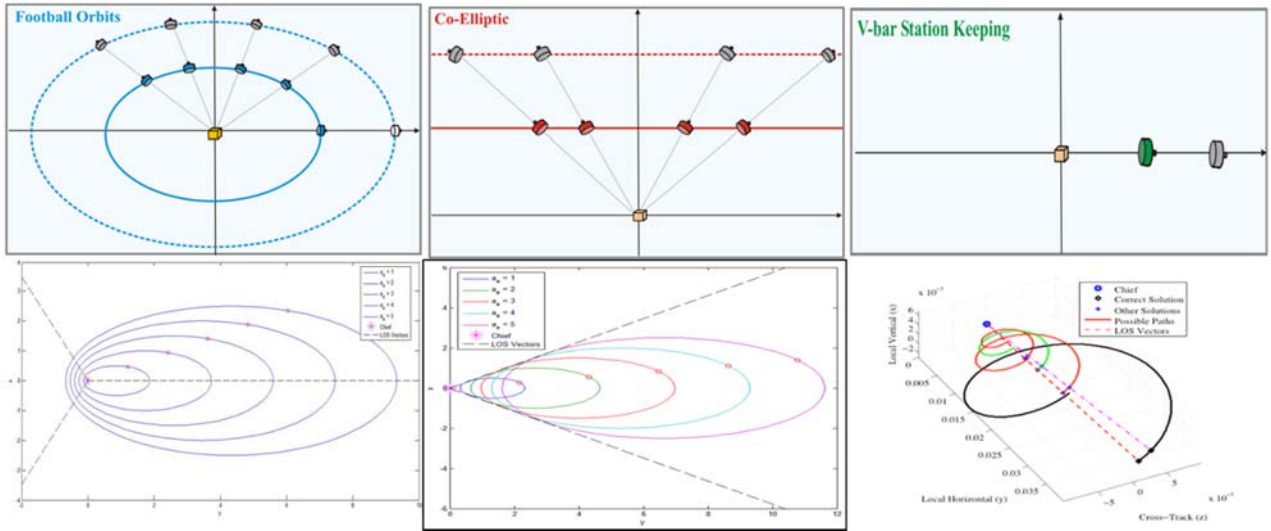


Figure 2. Various “Families” of Ambiguous Trajectories (all 5 Assumptions in Force)

3.1.2 Utilization of Nonlinear Dynamics

The first “relaxation” to be described is that of Assumption #1a above. Here all aspects of the scenario described in the previous section are in force, except that the relative motion between the observer and RSO are modeled with nonlinear dynamics. The nonlinear relative motion solution to be utilized is found [13-15]. This solution is similar to the Clohessy-Wiltshire solution in that it assumes two-body gravity and a circular chief orbit. However, instead of retaining only terms linear in the initial relative states, it retains second-order terms as well. The exact solution will not be repeated here, but it is of the following form:

$$\begin{aligned} x(t) &= C_1(t)x_0 + C_2(t)y_0 + \dots + C_6(t)\dot{z}_0 + C_7(t)x_0^2 + C_8(t)x_0y_0 + \dots + C_{27}(t)\dot{z}_0^2 \\ y(t) &= D_1(t)x_0 + \dots + D_{27}(t)\dot{z}_0^2 \\ z(t) &= E_1(t)x_0 + \dots + E_{27}(t)\dot{z}_0^2 \end{aligned} \quad (17)$$

Substituting for $x(t)$, $y(t)$, and $z(t)$ into Equation’s (14) at measurement time t_i yields

$$\begin{aligned} [-u_z(t_i)D_1(t_i) + u_y(t_i)E_1(t_i)]x_0 + \dots + [-u_z(t_i)D_{27}(t_i) + u_y(t_i)E_{27}(t_i)]\dot{z}_0^2 &= 0 \\ [u_z(t_i)C_1(t_i) - u_x(t_i)E_1(t_i)]x_0 + \dots + [u_z(t_i)C_{27}(t_i) - u_x(t_i)E_{27}(t_i)]\dot{z}_0^2 &= 0 \\ [-u_y(t_i)C_1(t_i) + u_x(t_i)D_1(t_i)]x_0 + \dots + [-u_y(t_i)C_{27}(t_i) + u_x(t_i)D_{27}(t_i)]\dot{z}_0^2 &= 0 \end{aligned} \quad (18)$$

If we obtain LOS measurements at n different times, our $3n$ measurement equations are coupled second-order polynomials in six unknowns (the six initial relative states). Note that these equations are not linear in the initial relative states, i.e. they cannot be written as $A\bar{x}_0 = 0$. Thus, if \bar{x}_0^* is a solution to these equations, $\alpha\bar{x}_0^*$ is not, i.e. we have escaped Woffinden’s dilemma by employing nonlinear relative dynamics. This situation is depicted in Figure 3. While these plots are notional (i.e. not actual propagated trajectories), they represent two initial state vectors (\bar{x}_0 and $\alpha\bar{x}_0$) propagated forward with nonlinear dynamics. The positions of the two objects relative to a chief at the origin are shown at four different times. While the LOS vectors of the objects are initially aligned, they deviate over time. Whereas if the objects’ motion were propagated with linear dynamics, their LOS histories would be identical for all time.

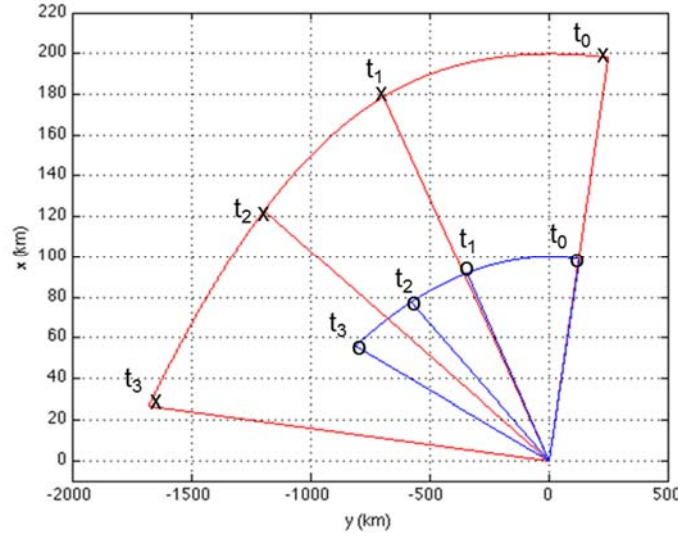


Figure 3. Notional Depiction of Two Trajectories Propagated with Nonlinear Dynamics

The issue that remains then is whether an efficient closed-form approach can be found to solve these equations. This is left for Section 3.

3.1.3 Utilization of Nonhomogeneous Dynamics

The next “relaxation” to be described is that of Assumption #1b. Here all aspects of the scenario described in the previous section are in force, except that the observer is not restricted to lie on the reference (chief) orbit during all the measurement times. As alluded to earlier, the case of a maneuvering observer is subsumed under this scenario.

Consider an RSO that performs a known maneuver Δv at time t_m . Further consider a LOS measurement of the RSO collected at time t_i after the maneuver. The solution for the relative position at t_i must now take into account the maneuver, thus Equation (4) becomes

$$\bar{r}(t_i) = [\Phi_{rr}(t_i, t_0) \quad \Phi_{rv}(t_i, t_0)] \bar{x}_0 + \Phi_{rv}(t_i, t_m) \Delta \bar{v} \quad (19)$$

The scenario more relevant to most proximity missions is that where the observer (whose motion is assumed known) performs the maneuver. This is easily accommodated in the same framework, but requires clarification of some details. Thus far, the state \bar{x} has been assumed to describe the position and velocity of the RSO relative to the observer at the origin of the LVLH frame. Alternatively, the origin of the LVLH frame can be considered to be an arbitrary object traveling along a two-body orbit. In such cases, the object will be referred to as the “virtual chief,” and its orbit as the “reference orbit.” While any orbit may serve as the reference orbit, it is often convenient to define the reference orbit based on the instantaneous ephemeris of the observer, then propagating that orbit forward to each measurement time with two-body dynamics. Obviously the observer will gradually deviate from this reference orbit (i.e. the origin of the LVLH frame) due to perturbations, but for a reasonable span of time, it will remain close to the LVLH origin until/unless it maneuvers.

Consider an observer initially located on the reference orbit. The observer then performs a known maneuver Δv at time t_m . Consider then a LOS measurement of the RSO collected at time t_i after the maneuver. The observer’s position at t_i is given by $\Phi_{rv}(t_i, t_m)\Delta v$, so the relative position between observer and RSO at t_i is shown below.

$$\bar{r}(t_i) = [\Phi_{rr}(t_i, t_0) \quad \Phi_{rv}(t_i, t_0)]\bar{x}_0 - \Phi_{rv}(t_i, t_m)\Delta\bar{v} \quad (20)$$

From Equations (19) and (20), we see that a known maneuver performed by either the RSO or observer will generally produce some nonhomogeneous change $\Delta\bar{r}$ in the relative position. For generality, both cases will be summarized as follows:

$$\bar{r}(t_i) = [\Phi_{rr}(t_i, t_0) \quad \Phi_{rv}(t_i, t_0)]\bar{x}_0 + \Delta\bar{r}(t_i) \quad (21)$$

Substitution into the measurement equations (14) produces the following:

$$\begin{bmatrix} 0 & -u_z(t_i) & u_y(t_i) \\ u_z(t_i) & 0 & -u_x(t_i) \\ -u_y(t_i) & u_x(t_i) & 0 \end{bmatrix} [\Phi_{rr}(t_i, t_0) \quad \Phi_{rv}(t_i, t_0)]\bar{x}_0 = - \begin{bmatrix} 0 & -u_z(t_i) & u_y(t_i) \\ u_z(t_i) & 0 & -u_x(t_i) \\ -u_y(t_i) & u_x(t_i) & 0 \end{bmatrix} \Delta\bar{r}(t_i) \quad (22)$$

Again, only two of the three equations are independent, but we may include all three equations without loss of generality. Collection of measurements at n instants produces a system of equations that can be written as $A\bar{x}_0 = b$. Note that if \bar{x}_0^* is a solution to these equations, $\partial\bar{x}_0^*$ is not, i.e. we have escaped Woffinden's dilemma by employing nonhomogeneous relative dynamics. This situation is depicted in Figure 4. Here LOS measurements are taken at t_1, t_2, t_3 , and t_4 , and the observer maneuvers at t_m between t_3 and t_4 . Because the maneuver takes the observer off the reference orbit, this will generally yield a different LOS at t_4 than would be obtained if the observer had not maneuvered, as shown by the green trajectory. In such a case, the observer's position vector in the LVLH frame (i.e. relative to the origin) is in fact the $\Delta\bar{r}$ represented in Equation (22). If, however, the observer's post-maneuver location happens to yield the *same* LOS at t_4 as if the observer had not maneuvered (as shown by the red trajectory), then the right-hand side of Equation (22) is zero (because $\hat{u}_r(t_4) \times \Delta\bar{r}(t_4) = 0$), thus the measurement equations remain homogeneous and no observability is gained. This type of maneuver will be referred to as a "singular" maneuver. Of course, the resulting $\Delta\bar{r}$ is a function of the relative trajectory, the maneuver time/magnitude/direction, and the post-maneuver measurement time. Therefore, if a given scenario results in a "red" trajectory at t_4 , an additional measurement at t_5 would likely yield observability. For p LOS measurements, A is a $3p \times 6$ matrix. If the matrix A is singular, there still will not be a unique solution (there will be either no solution or an infinite number of solutions), but if enough measurements are obtained such that A is full rank, a unique solution can be obtained via pseudoinverse:

$$\bar{x}_0 = (A^T A)^{-1} A^T b \quad (23)$$

It is worth re-emphasizing the point made at the beginning of this subsection: that a maneuver is not required to relax Assumption #1b. Rather, if the position history of either the RSO or observer relative to the reference orbit over the span of measurement times is such that, for whatever reason, it cannot be accurately described by homogeneous linear dynamics, then the measurement equations will be as given in Equation (22). Section 1 listed methods of relaxing Assumption #1b without maneuvering.

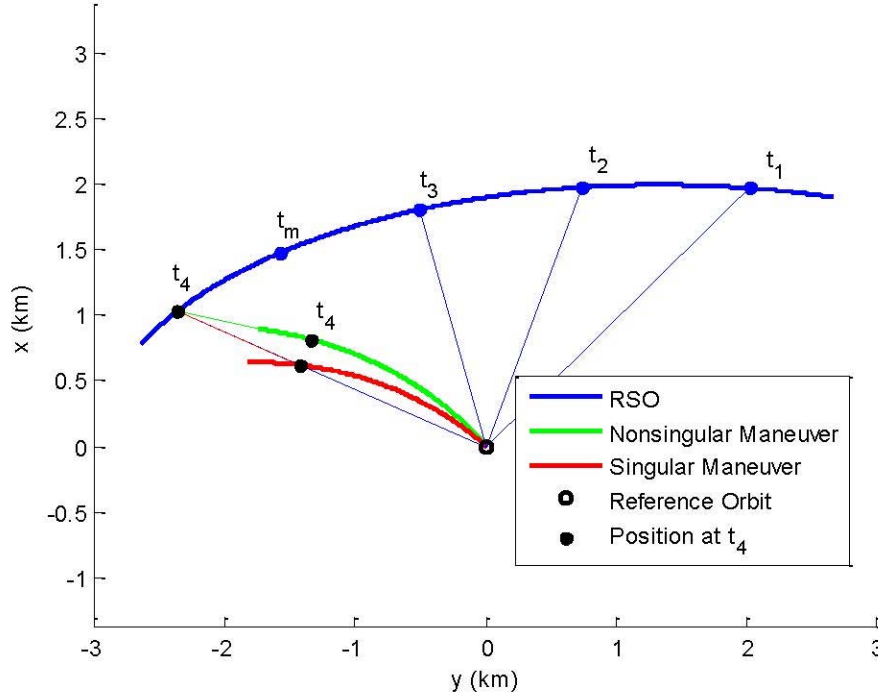


Figure 4. Notional Depiction of LOS Measurements Taken by Maneuvering Observer

3.2 Detailed Description of IROD Algorithms

Each IROD method estimates the 6 states corresponding to the trajectory of the observed object relative to the defined reference orbit at the epoch time, which is chosen to be the time of the first LOS measurement. In all cases, the observer's inertial ephemeris is assumed to be precisely known. The IROD algorithms take advantage of the relaxations of the conditions for guaranteed ambiguity that were described in Section 1. As described, the use of nonlinear dynamics produces a system of second-order polynomial equations, and the use of nonhomogeneous dynamics produces a system of nonhomogeneous linear equations. Solving a system of second-order polynomials is nontrivial, and two different methods were implemented and are described below in Subsections 3.2.1 and 3.2.2. Solving a system of nonhomogeneous linear equations is fairly straightforward, and the implementation of the method is described in Subsection 3.2.3.

3.2.1 Linear Matrix Method (LMM)

The Linear Matrix Method is a fairly ad-hoc approach to find an approximate solution to the system of second-order polynomials comprising the measurement equations in Equation (18). The method is a two-step procedure.

In the first step, each of the 27 possible linear and 2nd-order combinations of the six unknown variables (i.e., the unknown initial position and velocity components) are treated as independent unknowns. These 27 terms or “monomials” can be assembled into a vector $\bar{\chi}$:

Approved for public release; distribution is unlimited.

$$\bar{\chi} = [\chi_1 \quad \chi_2 \quad \chi_3 \quad \dots \quad \chi_{27}]^T \quad (24)$$

where, consistent with the ordering of terms in Equation (17) and (18), χ_1 corresponds to x_0 , χ_2 corresponds to y_0 , etc, and χ_{27} corresponds to \dot{z}_0^2 .

The measurement equations of Equation (18) are linear in the elements of $\bar{\chi}$, and can thus be recast as $A\bar{\chi} = 0$, where for n measurement times, A is a $3n \times 27$ matrix. From Equation (18) we see that

$$\begin{aligned} A_{11} &= -u_z(t_i)D_1(t_i) + u_y(t_i)E_1(t_i), \dots, A_{1,27} = -u_z(t_i)D_{27}(t_i) + u_y(t_i)E_{27}(t_i) \\ A_{21} &= u_z(t_i)C_1(t_i) - u_x(t_i)E_1(t_i), \dots, A_{2,27} = u_z(t_i)C_{27}(t_i) - u_x(t_i)E_{27}(t_i) \\ A_{31} &= -u_y(t_i)C_1(t_i) + u_x(t_i)D_1(t_i), \dots, A_{3,27} = -u_y(t_i)C_{27}(t_i) + u_x(t_i)D_{27}(t_i) \\ &\text{etc...} \end{aligned} \quad (25)$$

If A is less than full rank (i.e. singular), there is one nonzero solution for each degree of the null space of A . At first glance, this approach has not alleviated the range ambiguity because for each candidate solution $\bar{\chi}^*$, the scaling $\alpha\bar{\chi}^*$ is also a solution of $A\bar{\chi} = 0$. However, this ignores the quadratic relations between the elements of $\bar{\chi}$, i.e. in order for $\bar{\chi}^*$ to be a viable solution to the measurement equations, the 7th element of $\bar{\chi}^*$ must equal the square of the 1st element, etc. The second step of the method incorporates these constraints. After solving a null space vector of A (call it $\tilde{\chi}$), $\bar{\chi}$ is reformulated as:

$$\bar{\chi} = [\alpha\tilde{\chi}_1 \quad \alpha\tilde{\chi}_2 \quad \alpha\tilde{\chi}_3 \quad \alpha\tilde{\chi}_4 \quad \alpha\tilde{\chi}_5 \quad \alpha\tilde{\chi}_6 \quad \alpha^2\tilde{\chi}_1^2 \quad \alpha^2\tilde{\chi}_1\tilde{\chi}_2 \quad \dots \quad \alpha^2\tilde{\chi}_6^2]^T \quad (26)$$

where α remains to be solved. Note that this step involves discarding the 7th through 27th elements of $\tilde{\chi}$ (i.e. the elements pertaining to quadratic combinations of the unknowns). Each

element of the reformulated vector $\tilde{\chi}$ therefore contains α either linearly or quadratically. Substituting this vector back into the measurement equations, i.e. pre-multiplying by A , yields

$$\alpha A_{1-6} \begin{bmatrix} \tilde{\chi}_1 \\ \tilde{\chi}_2 \\ \tilde{\chi}_3 \\ \tilde{\chi}_4 \\ \tilde{\chi}_5 \\ \tilde{\chi}_6 \end{bmatrix} + \alpha^2 A_{7-27} \begin{bmatrix} \tilde{\chi}_1^2 \\ \tilde{\chi}_1 \tilde{\chi}_2 \\ \vdots \\ \tilde{\chi}_6^2 \end{bmatrix} = 0 \quad (27)$$

Here, A_{1-6} is a $3n \times 27$ matrix composed of the first 6 columns of A , and A_{7-27} is a $3n \times 21$ matrix composed of the 7th through 27th columns of A . This represents a set of $3n$ quadratic equations for α , the only remaining unknown. Each equation actually contains a trivial solution at $\alpha = 0$. Factoring α out leaves a set of linear equations for α :

$$A_{1-6} \begin{bmatrix} \tilde{\chi}_1 \\ \tilde{\chi}_2 \\ \tilde{\chi}_3 \\ \tilde{\chi}_4 \\ \tilde{\chi}_5 \\ \tilde{\chi}_6 \end{bmatrix} + \alpha A_{7-27} \begin{bmatrix} \tilde{\chi}_1^2 \\ \tilde{\chi}_1 \tilde{\chi}_2 \\ \vdots \\ \tilde{\chi}_6^2 \end{bmatrix} = 0 \quad (28)$$

At this point it should be noted that if there were no model error (i.e. if the reference orbit were perfectly known and the solution in Equation (17) were an exact representation of spacecraft dynamics) and no measurement error (i.e. if Equation (14) represented the exact relationship between the state values and measurement values), we would be guaranteed to find a solution to the measurement equations (Equation (18)) by the two-step process above. That is, at least one null space vector of A would be guaranteed to exist (call it $\tilde{\chi}^*$), and there would be a value of α (call it α^*) that, combined with $\tilde{\chi}^*$, would exactly solve each of the $3n$ equations in Equation (28). This solution would correspond to the exact values of the relative states at the epoch time, \bar{x}_0 . That is, the following equalities would hold:

$$\begin{aligned}
\alpha^* \tilde{\chi}_1^* &= x_0 \\
\alpha^* \tilde{\chi}_2^* &= y_0 \\
&\dots \\
\alpha^* \tilde{\chi}_6^* &= \dot{z}_0 \\
(\alpha^*)^2 \tilde{\chi}_1^{*2} &= x_0^2 \\
(\alpha^*)^2 \tilde{\chi}_1^* \tilde{\chi}_2^* &= x_0 y_0 \\
&\dots \\
(\alpha^*)^2 \tilde{\chi}_6^{*2} &= \dot{z}_0^2
\end{aligned} \tag{29}$$

where x_0 , y_0 , etc, are the true initial state values. However, due to model error and measurement error, we are *not* guaranteed that such a $\tilde{\chi}^*$ or α^* exists. The authors have simulated several cases with model error and/or measurement error, and a singular value decomposition of A shows that the matrix tends to have several singular values of approximately zero. That is, there are several right-singular vectors of A (of the form $\tilde{\chi}$) that approximately solve $A\tilde{\chi} = 0$. It is desired to explore which of these vectors leads to the “best” solution of Equation (18), where “best” is here defined as the solution that yields the minimum RMS residual angle error (defined below). Therefore, the LMM algorithm proceeds as follows:

- Given the LOS measurements and assuming the dynamics of Equation (17), construct the A matrix according to Equation (25)
- Perform a singular value decomposition of A
- For each of the 27 right-singular vectors $\tilde{\chi}$ of A , construct $\bar{\chi}$ according to Equation (26) and calculate the least-squares solution for α in Equation (28) (described below)
- For this candidate solution $\alpha\tilde{\chi}_{1-6}$, calculate the Root Mean Square (RMS) residual angle error by substituting these initial conditions into the second-order dynamics of Equation (17) (specifically the x , y , and z expressions) to produce a predicted position vector at each measurement time, $\bar{r}(t_i) = [x(t_i) \ y(t_i) \ z(t_i)]^T$, and evaluate the following expression:

$$\varepsilon = \sqrt{\frac{1}{n} \sum_{i=1}^n \left\{ \cos^{-1} \left[\frac{(r(t_i) \bullet \hat{u}_r(t_i))}{\|r(t_i)\|} \right] \right\}^2} \tag{30}$$

In Equation (30), $\hat{u}_r(t_i)$ is the actual (measured) LOS at t_i , and n is the number of measurement times. Thus, this residual metric is the RMS angle difference between the predicted and actual LOS values. The least-squares solution for α is calculated as follows:

$$\alpha = \frac{p^T q}{p^T p} \quad (31)$$

where $p = A_{7-27} \begin{bmatrix} \tilde{\chi}_1^2 \\ \tilde{\chi}_1 \tilde{\chi}_2 \\ \vdots \\ \tilde{\chi}_6^2 \end{bmatrix}$ and $q = -A_{1-6} \begin{bmatrix} \tilde{\chi}_1 \\ \tilde{\chi}_2 \\ \tilde{\chi}_3 \\ \tilde{\chi}_4 \\ \tilde{\chi}_5 \\ \tilde{\chi}_6 \end{bmatrix}$. Note that, since p and q are both 27 x 1 vectors,

Equation (31) represents a ratio of two scalars. Thus, of the 27 candidate solutions evaluated in the above process, the one selected as the IROD solution is that producing the lowest value of ε , which thus comes closest to satisfying the measurement equations, Equation (18). Whereas, the linear matrix method does not have a rigorous theoretical basis, simulation has shown it is capable of generating reasonable solutions in the presence of errors. While the authors concede that the A matrix will likely have several singular values significantly different than zero (which likely do not serve as good candidates for a solution), the reason for putting all 27 singular values through the above process is to emphasize the autonomous nature of the algorithm: rather than relying on a human-in-the-loop to evaluate whether each singular value of A is close enough to zero to merit consideration as a candidate solution, all singular values are given “equal opportunity” as candidate solutions.

Finally, some comment should be made regarding the number of LOS measurements the LMM algorithm requires. Technically, any number of measurements will allow the above steps to be followed in determining an IROD solution; because A is a $3n \times 27$ matrix, it will always have 27 right-singular vectors regardless the value of n . However, simulations have shown that for an adequate solution, measurements from at least 3 different times should be processed; given that each measurement time produces 2 independent measurements, this yields a number of independent measurements equal to the number of states. Additional measurements should provide incremental improvement.

3.2.2 Matrix Resultant Method (MRM)

Another approach implemented to solve the system of quadratic equations was based on the theory of resultant matrices, popularized by the work of Macaulay [16] and other mathematicians. Two significant differences between this and the linear matrix method are that (1) the MRM algorithm solves a square system of equations (number of measurements equal to number of relative states) and (2) the MRM algorithm is based on rigorous theoretical development in the literature.

To produce a square system of polynomial equations, two of the three equations generated at each measurement time (Equation 14) are selected. A method was implemented to select the most “independent” pair of equations. Each row of $U(t_i)$ is defined as a vector. Then, the norm of the cross product of each pair of vectors is calculated. The pair of components associated with the two vectors with the largest cross-product norm (i.e. the pair that is most “differently directed”) is chosen for inclusion in the matrix resultant method.

The specific implementation of Macaulay resultants to solve a system of n polynomials in n variables was based on [17]. However, a general overview of the method is provided here. The method begins by selecting a root variable that will be solved for first. The method is somewhat similar to the linear matrix method, in that the higher-order combinations of the remaining unknown variables are treated as independent unknowns and the equations are therefore treated as linear. Additional equations to solve for these remaining unknowns are generated by multiplying the original equations by various polynomial combinations of the original unknowns, until a square system is reached. This raises the overall order of the system, and can result in a large system of equations. However, the generation of additional equations is carefully designed so that the solutions for the additional unknowns automatically satisfy the polynomial constraints among them (i.e., no discard & recombine step is necessary, as is performed in the linear matrix method).

The result is a homogeneous system of linear equations for the polynomial equations of the remaining unknowns, where the coefficients are functions of the root variable. The existence of a solution requires that the matrix of coefficients is singular, which can be posed as a generalized eigenvalue problem. Solving this generalized eigenvalue problem produces multiple solutions for the root variable, many of which are infinite. Substituting each finite value of the root variable one at a time into the matrix of coefficients and solving for the null vector of the system provides solutions for the remaining unknown variables (again, for each value of the root variable).

For the solution of six quadratic equations for the six unknown initial states, the resulting generalized eigenvalue problem is 1584×1584 . Solution of this problem using the standard precision in MATLAB has been seen to result in large errors in the resulting solution. Therefore, an alternative method was implemented based on concepts introduced in [18]. If the initial (epoch) time is chosen as the time of the first LOS measurement, then the following linear transformation can be substituted for the initial position components:

$$\vec{r}(t_0) = r_0 \hat{u}_r(t_0) \quad \text{or} \quad \begin{bmatrix} x_0 \\ y_0 \\ z_0 \end{bmatrix} = r_0 \begin{bmatrix} u_x(t_0) \\ u_y(t_0) \\ u_z(t_0) \end{bmatrix} \quad (32)$$

Thus, the three unknowns x_0 , y_0 , and z_0 , can be linearly replaced by the single unknown r_0 . Then, the most “independent” pair of components at two additional measurement times are used to solve for the remaining four unknowns: r_0 and the three initial velocity components \dot{x}_0 , \dot{y}_0 , and \dot{z}_0 . The three equations generated at each measurement are similar to Equation (18), but reformulated in terms of the new unknowns:

$$\begin{aligned} & \left[(-u_z(t_i)D_1(t_i) + u_y(t_i)E_1(t_i))u_x(t_0) + (-u_z(t_i)D_2(t_i) + u_y(t_i)E_2(t_i))u_y(t_0) \right. \\ & \left. + (-u_z(t_i)D_3(t_i) + u_y(t_i)E_3(t_i))u_z(t_0) \right] r_0 + \dots + \left[-u_z(t_i)D_{27}(t_i) + u_y(t_i)E_{27}(t_i) \right] \dot{z}_0^2 = 0 \\ & \left[(u_z(t_i)C_1(t_i) - u_x(t_i)E_1(t_i))u_x(t_0) + (u_z(t_i)C_2(t_i) - u_x(t_i)E_2(t_i))u_y(t_0) \right. \\ & \left. + (u_z(t_i)C_3(t_i) - u_x(t_i)E_3(t_i))u_z(t_0) \right] r_0 + \dots + \left[u_z(t_i)C_{27}(t_i) - u_x(t_i)E_{27}(t_i) \right] \dot{z}_0^2 = 0 \\ & \left[(-u_y(t_i)C_1(t_i) + u_x(t_i)D_1(t_i))u_x(t_0) + (-u_y(t_i)C_2(t_i) + u_x(t_i)D_2(t_i))u_y(t_0) \right. \\ & \left. + (-u_y(t_i)C_3(t_i) + u_x(t_i)D_3(t_i))u_z(t_0) \right] r_0 + \dots + \left[-u_y(t_i)C_{27}(t_i) + u_x(t_i)D_{27}(t_i) \right] \dot{z}_0^2 = 0 \end{aligned} \quad (33)$$

This implementation is referred to as the separation-magnitude formulation. The solution of four quadratic equations for these four unknowns results in a generalized eigenvalue problem of 112 x 112. Solution of this problem results in significantly less loss of precision than the 1,584 x 1,584 scenario described above.

Some discussion is in order regarding the number of solutions yielded by the matrix resultant method. According to Bezout's Theorem [19], there are a^b solutions to a system of coupled polynomials, where a represents the order of each polynomial and b represents the number of polynomials (i.e. number of variables). For four 2nd-order polynomials, the number of solutions is then 16. However, these solutions are in the complex domain, i.e. it is possible that each solution may consist of one or more values with imaginary parts. There is no known theorem for how many real solutions may exist, so the best that can be said is that the *maximum* number of real solutions for a given scenario is 16.

Unlike the infinite ambiguity associated with Woffinden's dilemma, here we have a finite ambiguity to deal with. Disambiguation of the (potentially) multiple real solutions is fairly straightforward. First, the measurement equations require that the relative position vector at each measurement time be parallel to the LOS. This can result in solutions that contain relative position vectors that are pointing the wrong direction (180° opposed to the LOS measurement) at one or more measurement times. For each solution, the propagated relative position vector can be checked, and if it points in the wrong direction at any measurement time, the solution can be discarded. At this point, there may still be multiple real solutions that satisfy the measurement equations. However, experience shows that all but one of the remaining solutions are physically unrealistic, i.e. containing separation magnitudes (i.e. observer-to-RSO range values) far beyond the domain of applicability of the second-order solution. Thus, the one realistic solution would be considered the "winner" for this algorithm.

3.2.3 Nonhomogeneous Observer Method (NOM)

The final IROD algorithm takes advantage of the observability provided by a nonhomogeneous observer, as described in the previous section. The method uses data for the LOS vector from the observer to the RSO and the relative position vector of the observer relative to the reference orbit (both expressed in the reference orbit's LVLH components). The method assumes that the observer does not lie on the reference orbit during all the measurement times. If this condition is met (for example) by the observer performing maneuvers during the span of the measurements, then the number of maneuvers, exact sequencing of the maneuvers within the measurements, and magnitude and direction of the maneuvers do not need to be explicitly input into the algorithm. Rather, one simply needs the observer's position relative to the reference orbit at each measurement time resulting from the maneuvers; this is $\Delta\vec{r}(t_i)$ as represented in Equation (21). As described previously, the method results in a linear system of equations, $A\bar{x}_0 = b$, for the unknown initial conditions, which can be solved by taking a pseudoinverse. So, whereas three independent LOS measurements (resulting in six measurement equations) are required for A (and therefore its pseudoinverse) to be full rank, there is no upper limit on how many LOS measurements can be incorporated. Any number of measurements beyond three results in a least-squares solution for \bar{x}_0 . It should be noted that in a real scenario, error will exist in the observer's position. Because the NOM method does not account for this error, it may be falsely attributed to nonhomogeneous motion and thus create a false sense of observability. That is, if the observer deviates from the defined reference orbit due to position knowledge error, the NOM method will assume this deviation is due to a maneuver. Therefore, in order for NOM to be effective, the maneuver (or other nonhomogeneous observer activity) must induce "true" nonhomogeneous

motion that is greater than the “false” nonhomogeneous motion induced by the aforementioned errors.

3.2.4 Practical Considerations

Practical issues arise when performing the various IROD schemes detailed above. Some of these issues are as follows:

Eccentricity in the reference orbit: While the NOM method allows for an elliptical reference orbit, the LMM and MRM methods assume the reference orbit is circular. For most scenarios of interest, this is not expected to be a problem for the LMM and MRM methods. Typically, relative motion is driven more by the eccentricity difference between the “chief” and “deputy” orbits than by the eccentricity in the chief orbit itself (in fact, it is the eccentricity difference that causes the relative trajectory to resemble a 2 x 1 ellipse in the radial/along-track plane). Simulations show that when the chief and deputy orbits both have small nonzero eccentricity, the relative trajectory closely resembles that for a circular chief orbit (e.g. the 2 x 1 ellipse). Thus, it is expected that orbit eccentricity will not be a major issue when applying the LMM and MRM methods herein.

Spatial and temporal regions of applicability for each method: It is expected that there are both an upper and lower limit on the time span of measurements for which the above methods will be effective. This is because the shorter the time between first and last measurement, the less of a “look” the method gets at the orbit, while the longer this time interval, the more probability there is for an propagation error to build up between the dynamic model assumed by these methods and real motion in space. Similarly, there is expected to be an upper and lower limit on the separation between the chief and deputy orbits (specifically, between the reference orbit and the orbit of the RSO being observed), in terms of where the above methods will be effective. This is because the closer these two orbits are, the more the relative motion between them appears linear. In such “quasi-linear” conditions, it will likely be difficult to determine the proper magnitude (i.e. scaling) of the relative trajectory, even with methods designed to prevent Woffinden’s dilemma (such as the above methods). Conversely, the more different the two orbits are, the more nonlinear the relative motion between them will be. For example, there could be a scenarios where a closed-form expression of the relative motion between two objects may require 3rd-order or higher terms to accurately represent the motion. In such cases, the above methods likely would not perform well because the models assumed in those methods do not accurately represent the motion. Thus, in both the spatial and temporal sense, there is an acceptable region, or “sweet spot,” where the methods should perform well.

3.3 Description of Scenarios

Before delineating the various scenarios, it is useful to reiterate the following properties of the IROD algorithms:

- Each algorithm assumes knowledge of the observer location at each measurement time, and in most cases the reference orbit (in whose frame the relative solution is expressed) is defined based on this knowledge.

- The algorithms require *no* knowledge of the observed object (orbit, shape/geometry, etc.), other than the line-of-sight measurements to the object; any ephemeris information of the observed object (e.g., on-board telemetry or external solutions) is used strictly for verification.
- Two of the algorithms do not incorporate maneuvers by the observer, while one of the algorithms does; all three algorithms assume the observed object is *not* maneuvering.

There are three general categories of scenarios explored herein:

- *Relative approach to classical (ground-based) IOD*: Performance of IROD algorithms utilizing ground sensor data
- *Close-proximity IROD*: Performance of IROD algorithms utilizing space-based sensor data

3.3.1 Ground-Based IROD (GIROD)

In Subsection 3.1.3, it was described how observability can be induced if the observer does not lie along the defined reference orbit during all the measurement times. This will be referred to here as the “nonhomogeneous condition.” The NOM method described previously was constructed based on this condition. Specifically, the nonhomogeneous condition is that the observer’s motion relative to the reference object (“virtual chief”), when expressed in the LVLH frame of the reference object, does not obey linear dynamics. This condition was first described in the context of a maneuvering observer, since this is quite an obvious example of the condition. It turns out that any observer actually meets this condition whether it is maneuvering or not, since its (real) motion relative to any defined two-body reference orbit is not linear. However, because this relative motion is of very small magnitude (i.e. an observer’s orbit is generally very close to a neighboring two-body reference orbit), this is a “quasi-homogeneous” scenario. That is, the observer’s motion relative to the virtual chief would add little to no observability (i.e. the proper scale factor of the motion could likely not be determined with any accuracy). One type of scenario that meets the nonhomogeneous condition quite well is that of conventional ground-based tracking, where the observer is a sensor on the Earth.

To apply IROD to ground-based tracking data, the measurement equations are of the form in Equation (22). Typically, data for an optical ground sensor consists of right ascension and declination of the line-of-sight from the sensor to the object expressed in some familiar coordinate frame, e.g. Earth-Centered Inertial (ECI) at each measurement time. In addition, the sensor's location on the Earth is known, typically in terms of latitude, longitude, and altitude. Given this information, once a reference object and orbit are defined, the vector from the sensor to the reference object ("virtual chief") in the reference object's LVLH frame can be kinematically derived at each measurement time. This vector is then $\Delta\bar{\mathbf{r}}(t_i)$ in Equations (21) and (22). The NOM method can then be used to determine the orbit of the observed object in the reference object's LVLH frame, i.e. the solution. Note: That GIROD constitutes a relative approach to the classical (ground-based) IOD problem.

3.3.2 Close-Proximity IROD (CIROD)

For these scenarios, various sets of LOS measurements from a space-based observer to an RSO are chosen, and each of the IROD algorithms will be used to process the measurements. Cases are simulated that include one or more maneuvers interspersed between the measurements, as well as measurement sets involving no maneuvers. Cases are chosen involving various time spans from initial to final measurement, as well as varying degrees of separation between observer and RSO. The purpose here is not only to explore the general accuracy of the IROD algorithms, but also the limits of the acceptable region (both spatially and temporally) described above.

3.3.3 Delineation of IROD test cases

The various test cases to be demonstrated in the above two scenarios are characterized by variation of the following parameters, as detailed in Table 1:

- Whether 1st-order (NOM) or 2nd-order (LMM or MRM) relative dynamics are assumed in the IROD algorithm
- The choice of observer: either an observer satellite or a ground sensor
- The basis for choosing the reference orbit: either the observer ephemeris or a "virtual" reference orbit

Table 1. The Three Possible Delineations of Test Case Parameters in the Experiments to Follow

Dynamics order	Observer	Observed object	Reference object/orbit	# of measurements	timeline
1 st (NOM)	ground sensor	RSO	virtual	(variable)	(variable)
1 st (NOM)	observer satellite	RSO	observer satellite	(variable)	(variable)
2 nd (LMM or MRM)	observer satellite	RSO	observer satellite	(variable)	(variable)

Regarding the third bullet, the reference orbit may be constructed in two ways. The first method is by obtaining an ephemeris for the observer just prior to the first measurement time, and propagating that ephemeris forward with two-body dynamics. An “ad-hoc” method of reference orbit construction is based only on the LOS measurements and the assumption that the observed object is in a near-geosynchronous object. Using the observer’s location, the intersection is calculated of the first LOS measurement with a sphere centered at the center of the Earth and radius equal to the geosynchronous semi-major axis. The reference orbit at the initial epoch is positioned at the location of this intersection:

$$\bar{R}(t_0) = \bar{R}_{obs}(t_0) + c\hat{u}_r(t_0) \quad (34)$$

$$\bar{R}^T(t_0)\bar{R}(t_0) = a_{Geo}^2 \quad (35)$$

$$\alpha^2 + 2\hat{u}_r^T(t_0)\bar{R}_{obs}(t_0)\alpha + \bar{R}_{obs}^T(t_0)\bar{R}_{obs}(t_0) - a_{Geo}^2 = 0 \quad (36)$$

The positive solution for α corresponds to the desired intersection. The reference orbit at the initial epoch is positioned at the location of this intersection. The velocity of the reference orbit at this epoch is chosen with magnitude equal to that of a circular geosynchronous orbit and direction perpendicular to the initial position vector and parallel to the equatorial plane:

$$\bar{V}^T(t_0)\bar{V}(t_0) = \frac{\mu}{a_{Geo}} \quad (37)$$

$$\bar{V}(t_0) = \pm \sqrt{\frac{\mu}{a_{Geo}}} \frac{\hat{K} \times \bar{R}(t_0)}{\|\hat{K} \times \bar{R}(t_0)\|} \quad (38)$$

where \hat{K} is the unit vector in the direction of Earth's polar axis. To select from the two possible parallel directions, the velocity is chosen to be generally in the direction of the second LOS measurement. This method is equivalent to selecting the reference orbit to be circular and geosynchronous, with inclination equal to the latitude of the observed object at the initial epoch, i.e. the reference orbit is assumed to be at its maximum absolute latitude at the initial epoch.

The results shown in Section 4 illustrate the use of IROD techniques for ground-based tracking scenarios and close-proximity scenarios, each as a function of the various parameter choices detailed above and in Table 1.

3.4 Data Requirements for Scenarios, with Description of Data Flow

This section describes the specific inputs required for each of the scenario categories, the output (solution) information provided, and the flow of data through each IROD algorithm from inputs to output. This structure is dictated largely by the delineation of IROD test cases detailed above.

3.4.1 GIROD

3.4.1.1 Input Structure

Following are the inputs required for the ground-based IROD scenarios:

- LOS measurements from ground sensor to observed object, expressed as right ascension and declination in the ECI coordinate frame
- Time of each aforementioned LOS measurement
- Ground sensor latitude, longitude, and altitude at time of each LOS measurement
- Reference orbit information, constructed from the LOS measurements via Equation's 34-38

3.4.1.2 Data Flow (from Inputs to Output)

Figure 5 illustrates how the above inputs are manipulated for processing to yield an IROD solution. The GIROD environment consists of two main MATLAB scripts: Pre_Process_Data.m, and Ground-Based_IROD.m, which are executed sequentially. These scripts are further described in the following paragraphs.

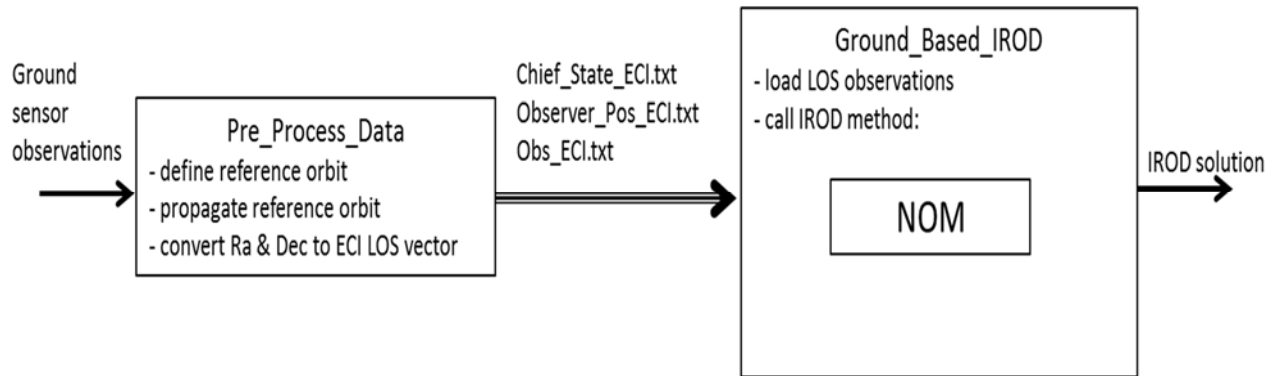


Figure 5. Flow Chart of Ground-based IROD Algorithmic Process

3.4.1.2.1 Pre_Process_Data.m:

The main purposes of Pre_Process_Data.m are (1) to compute ground sensor LOS (right ascension and declination) measurements of the observed object in the LVLH frame of the reference orbit and (2) to compute the vector from the sensor to the reference object (“virtual chief”) in the reference object’s LVLH frame at each measurement time. The reference orbit is derived from the LOS measurements via Eqn’s 34-38. The reference object is then propagated to each of the ground sensor measurement times using two-body (Keplerian) dynamics so that the ground sensor measurements can be converted from the ECI frame to the LVLH frame. This script also loads a high fidelity ephemeris for the location of the ground sensor in the ECI frame, which also is converted at each measurement time to the LVLH frame. The output of Pre_Process Data.m is data files in text format with the reference orbit ECI states, the LVLH relative position vector of the ground sensor at each measurement time, and the LOS vectors expressed in LVLH at each measurement time.

3.4.1.2.2 Ground_Based_IROD.m:

Ground_Based_IROD.m loads the aforementioned data files from Pre_Process Data.m. The IROD solution is then calculated using the Nonhomogeneous Observer Method. The specific output data is described in a later subsection.

3.4.2 CIROD

3.4.2.1 Input Structure

Following are the inputs required for the close-proximity IROD scenarios (all quantities are assumed to be obtained from on-board telemetry):

- LOS measurements from observer to RSO, expressed in observer camera frame
- Time of each aforementioned LOS measurement
- Direction cosine matrix from observer camera frame to observer body frame
- Latest available observer rotational ephemeris (i.e. attitude estimate) before each LOS measurement, with time tags
- Observer attitude rate (i.e. angular velocity) estimate before each LOS measurement, with time tags
- Reference orbit information (i.e. time and ephemeris of observer) prior to the first LOS measurement

If the NOM IROD method is employed, an additional input is the latest available observer orbit ephemeris before *each* LOS measurement, with time tag.

3.4.2.2 Data Flow (from Inputs to Output)

Figure 6 illustrates how the above inputs are manipulated for processing to yield an IROD solution. Generally, the description provided in this subsection applies to all three IROD algorithms. The CIROD environment consists of three main MATLAB scripts: `Save_Struct_Variables.m`, `Pre_Process_Cam_Data.m`, and `Close_Proximity_IROD.m`, which are executed sequentially. These scripts are further described in the following paragraphs.

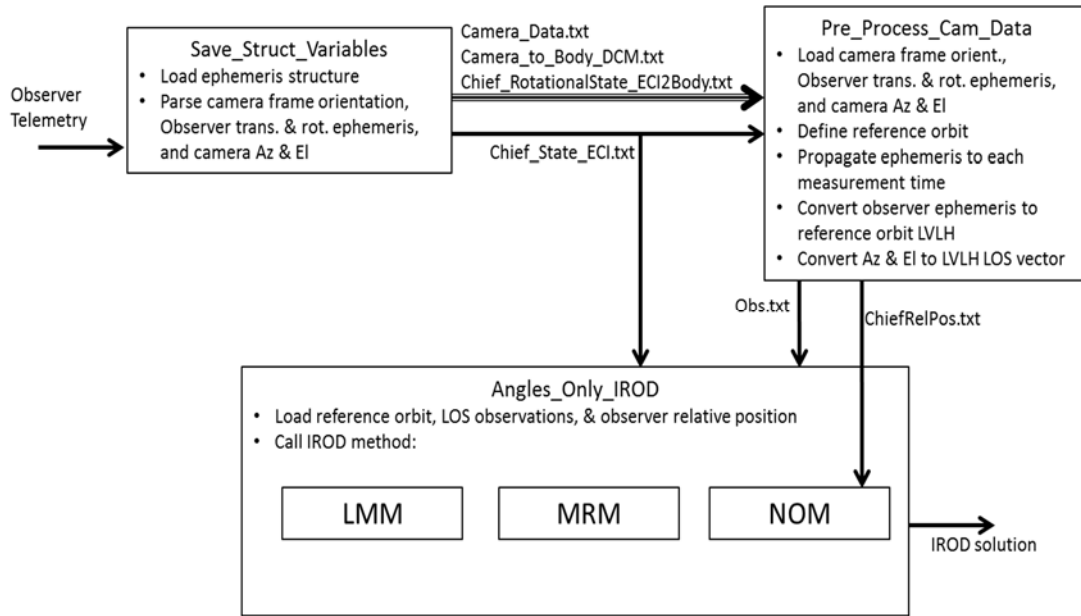


Figure 6. Flow Chart of Close-proximity IROD Algorithmic Process

3.4.2.2.1 Save_Struct_Variables.m:

Save_Struct_Variables.m loads the observer telemetry. As detailed above, these data types are the observer inertial (translational) ephemeris information, rotational ephemeris information, orientation of the camera frame relative to the body frame, and azimuth and elevation measurements of the RSO in the camera frame. It is assumed that this data exists in the form of a MATLAB structure. Save_Struct_Variables.m parses this structure into separate text files for each data type.

3.4.2.2.2 Pre_Process_Cam_Data.m:

The main purpose of Pre_Process_Cam_Data.m is to convert observer azimuth and elevation measurements of the RSO (originally expressed in the observer camera frame) to LOS vector components in the LVLH frame of the reference orbit. Thus, the inputs to this script are text files (generated from Save_Struct_Variables.m) for the azimuth and elevation measurements and associated times, camera frame orientation relative to the observer body frame, and the inertial ephemeris for the observer translational and rotational motion at various times.

The reference orbit is defined by propagating the first observer ephemeris forward with two-body dynamics. Here, “first” is defined to be the latest available ephemeris before the first LOS measurement time. Since the observer will not follow the (two-body) reference orbit precisely, the object whose motion defines the LVLH frame is in fact a “virtual chief,” as described previously. Each camera frame azimuth and elevation measurement is then converted into a LOS vector in LVLH components via the following steps:

- Express Az/El as a LOS vector in the camera frame:

$$\hat{\mathbf{u}}_r^{cam} = \begin{bmatrix} \cos(\text{WFOVMEASEL})\sin(\text{WFOVMEASAZ}) \\ \sin(\text{WFOVMEASEL}) \\ \cos(\text{WFOVMEASEL})\cos(\text{WFOVMEASAZ}) \end{bmatrix} \quad (39)$$

- Convert the camera frame representation of the LOS vector into a body frame representation via the direction cosine matrix between the two frames:

$$\hat{\mathbf{u}}_r^{body} = T_{cam2body} \hat{\mathbf{u}}_r^{cam} \quad (40)$$

(where the elements of $T_{cam2body}$ are obtained from telemetry)

- Convert the body frame representation of the LOS vector into an ECI representation via the direction cosine matrix between the two frames:

$$\hat{\mathbf{u}}_r^{ECI} = T_{body2ECI} \hat{\mathbf{u}}_r^{body} \quad (41)$$

(where the elements of $T_{body2ECI}$ are derived from quaternions using formulas from [20])

- Convert the ECI representation of the LOS vector into an LVLH representation via the direction cosine matrix between the two frames:

$$\hat{u}_r^{LVLH} = T_{ECI2LVLH} \hat{u}_r^{ECI} = \begin{bmatrix} \frac{\bar{r}_{VC}}{|\bar{r}_{VC}|} & \frac{(\bar{r}_{VC} \times \bar{v}_{VC}) \times \bar{r}_{VC}}{|\bar{r}_{VC} \times \bar{v}_{VC}| \times |\bar{r}_{VC}|} & \frac{\bar{r}_{VC} \times \bar{v}_{VC}}{|\bar{r}_{VC} \times \bar{v}_{VC}|} \end{bmatrix}^T \hat{u}_r^{ECI} \quad (42)$$

(where \bar{r}_{VC} and \bar{v}_{VC} are the inertial position and velocity vectors of the virtual chief, i.e. reference object, at each measurement time, expressed in ECI coordinates)

Two important details should be pointed out here. First, regarding Equation (41), because the times associated with the observer ephemeris data generally are not the same as the “frame times” corresponding to the azimuth and elevation measurements, each rotational ephemeris (i.e. attitude estimate) is propagated from its epoch time to the proper measurement time in order to calculate $T_{body2ECI}$. Namely, for each measurement time t_i , the latest available quaternion values before time t_i are propagated forward to t_i . This propagation assumes constant angular velocity, i.e. the values of the angular velocity vector components reported at the time of the above-mentioned quaternions are taken to be constant from the time they are reported until time t_i .

Second, regarding Equation (42), the virtual chief and its reference orbit are used to calculate $T_{ECI2LVLH}$ at each measurement time, rather than using the latest available observer translational ephemeris, as is done with the rotational ephemeris above. However, when utilizing the “nonhomogeneous observer” (NOM) algorithm described above, the latest available observer translational ephemeris is in fact propagated to each measurement time. This is so that the relative position of the observer with respect to the reference orbit (i.e. virtual chief) can be computed at each measurement time (this is in fact the $\Delta \bar{r}(t_i)$ term in Equation (21)). Note that until the observer performs a maneuver during the span of measurements (or if it does not perform any maneuvers at all), each $\Delta \bar{r}(t_i)$ will be due only to propagation error between the actual and the two-body predicted location of the observer.

The output of Pre_Process_Cam_Data.m is data files in text format with the relative position vector of the observer with respect to the reference orbit at each measurement time (in the event the user chooses the NOM method in the next script) and the LOS vector from the observer to the observed object at each measurement time; all vectors are expressed in the LVLH frame of the reference orbit.

3.4.2.2.3 Close_Proximity_IROD.m:

Close_Proximity_IROD.m loads data files for the observer's inertial ephemeris (obtained from Save_Struct_Variables.m) and the LOS vectors (obtained from Pre_Process_Cam_Data.m). This script then asks the user to select one of the three IROD algorithms described in Section 3.2 (LMM, MRM, or NOM). If the nonhomogeneous observer method is selected, then the data file for the observer's relative position vector is also loaded. The output of Close_Proximity_IROD.m is the IROD solution; the specific output data is described in the subsection below.

3.4.3 Output Metrics and Verification

Once the chosen IROD algorithm is finished executing, the solution is output to the command window (and saved to a data file) in several formats, including:

- Relative states of the observed object in the LVLH frame of the reference orbit, at the epoch time (e.g. first measurement time)
- Relative orbit elements of the observed object (described below), at the epoch time
- ECI position and velocity of the observed object, at the epoch time
- Classical orbital elements of the observed object

The RMS residual angle error described in Equation (30) is also displayed and written to a file. Additionally, plots of the solved relative-motion trajectory are generated, overlaid with the LOS measurements and perhaps with the simulated truth (2-body) trajectory. For each test case explored in the Results section, various metrics chosen from those above will be displayed.

3.4.4 Relative Orbit Elements

Relative Orbit Elements (ROEs) are a geometric description of relative motion between two space objects, termed the “chief” and “deputy.” ROEs are analogous to classical orbital elements, which describe two-body inertial motion of a single object. The ROE formulation adopted here first appeared in [21-22]. This particular ROE set serves as a re-parameterization of the Clohessy-Wiltshire solution, under which the motion can be generally described as a drifting 2x1 ellipse in the x-y (radial/along-track) plane, with sinusoidal motion in the z (cross-track) direction superposed. The conversion from Cartesian relative states $\begin{bmatrix} x & y & z & \dot{x} & \dot{y} & \dot{z} \end{bmatrix}^T$ to ROEs is as follows:

$$\begin{aligned}
a_e &= 2\sqrt{\left(\frac{\dot{x}}{n}\right)^2 + \left(3x + 2\frac{\dot{y}}{n}\right)^2} \\
x_d &= 4x + 2\frac{\dot{y}}{n} \\
y_d &= y - 2\frac{\dot{x}}{n} \\
\beta &= \text{atan2}(\dot{x}, 3nx + 2\dot{y}) \\
z_{\max} &= \sqrt{\left(\frac{\dot{z}}{n}\right)^2 + z^2} \\
\gamma &= \text{atan2}(nz, \dot{z}) - \beta
\end{aligned} \tag{43}$$

where a_e is the length of the semi-major axis of the 2x1 ellipse, x_d is the radial distance of the center of the ellipse above or below the y (along-track) axis, y_d is the along-track distance of the center of the ellipse ahead or behind the x (radial) axis, β is the anomaly angle indicating the deputy's location in its relative orbit, z_{\max} is the amplitude of the sinusoidal cross-track motion, and γ is the phase difference between the radial/along-track motion and cross-track motion. Under the assumptions of Clohessy-Wiltshire motion, a_e , x_d , z_{\max} , and γ remain constant while β and y_d vary linearly with time. For real scenarios, this will not be the case, but it is still useful at any point in a scenario to convert the Cartesian relative states to ROEs in order to get an instantaneous “snapshot” of the geometry of the relative orbit. It is also instructive to explore how “Woffinden’s Dilemma” affects ROE values. As was done in a previous section, consider two trajectories, one whose values at t_0 are given by \bar{x}_{01} and the other whose initial values are $\bar{x}_{02} = \alpha\bar{x}_{01}$, where α is a positive real number. At any given time t , the value of a_e for the two trajectories are related by:

$$a_{e2} = 2\sqrt{\left(\frac{\dot{x}_2}{n}\right)^2 + \left(3x_2 + 2\frac{\dot{y}_2}{n}\right)^2} = 2\sqrt{\left(\frac{\alpha\dot{x}_1}{n}\right)^2 + \left(3\alpha x_1 + 2\frac{\alpha\dot{y}_1}{n}\right)^2} = \alpha a_{e1} \tag{44}$$

Thus we see that a_e scales with α . It can also be shown that x_d , y_d , and z_{\max} scale with α , while β and γ remain unchanged regardless the value of α . Recall this type of ambiguity was previously described as an infinite “family” of trajectories possessing the same line-of-sight history, whose (Cartesian) relative state values at any given time are scale multiples of one another. In terms of ROEs, we can say that this family of trajectories all possess the same β and γ history, while a_e , x_d , y_d , and z_{\max} of these trajectories are related by scale multiples.

Consider in particular the ROEs that remain constant (a_e , x_d , z_{\max} , and γ). Suppose we have “truth” knowledge of a relative orbit via Two-line Element (TLE), Global Positioning System (GPS), etc., we utilize one of the IROD methods to obtain an estimate for the orbit, and we want to evaluate the accuracy of our solution. At any chosen time, suppose we evaluate the ROE values for both the “truth” orbit and the estimated orbit. If the estimate captures the proper “family” of the true trajectory but fails to capture the proper “ α ” scale factor, the ratio of the estimated value of a_e to

the “true” value of a_e , the ratio of the estimated x_d to the “true” x_d , and the ratio of the estimated z_{max} to the “true” z_{max} should all be nearly equal. That is:

$$\frac{a_{e,est}}{a_{e,true}} \approx \frac{x_{d,est}}{x_{d,true}} \approx \frac{z_{max,est}}{z_{max,true}} \quad (45)$$

If in fact the estimate captures the proper scale factor as well, these ratios will be near 1. In the case of γ , because this parameter remains constant under Clohessy-Wiltshire assumptions and remains unchanged regardless the value of α , this means that as long as the estimate at least captures the proper “family” of the true trajectory, the γ ratio should be near 1. Note that if the space objects in the scenario behaved according to Clohessy-Wiltshire motion rather than real motion, the ratios in Equation (45) would be exactly equal (specifically 1 if the estimate were to capture the proper scale factor), and the γ ratio would be exactly 1. Because of their usefulness in assessing the quality of an IROD solution, ROE ratios will be evaluated for many of the scenarios detailed in the next section.

4 RESULTS AND DISCUSSION

Several test cases have been explored, within the two categories delineated in Section 3 and employing various combinations of the parameters outlined in Table 1. For each test case, some basic details of the case are given, including the number and time span of the measurements, a brief description of the space objects' motion, and the combination of Table 1 parameters employed. Results are presented in terms of the various metrics outlined in the previous section.

4.1 GIROD

These results are based on simulated ground observations (i.e. LOS measurements) of a space object during a single night of viewing. The chosen location of the sensor is 35°N lat, 111°W long (near Flagstaff, AZ). To represent a realistic sensor, a small amount of Gaussian error was added to each LOS measurement.

4.1.1 GIROD Scenario 1

**Table 2. Description of GIROD Scenario 1, Including Table 1
Parameter Values**

Dynamics order	Observer	Observed object	Reference object/orbit	# of measurements	Time span
1 st (NOM)	ground sensor	RSO	virtual	243	4hrs 41min

The IROD approach formulates the problem as solving for the motion of the RSO relative to a reference orbit. In this scenario, the reference orbit is constructed using the ad-hoc method described in Equation's (34)-(38), based on LOS measurement data for the RSO. Table 2 gives a basic description of this case. The orbital elements of the resulting reference orbit are shown in Table 3, row (a). The IROD solution is computed using 243 observations.

The IROD solution, together with the constructed reference orbit, can be kinematically transformed to compute a solution for the inertial orbit of the RSO. Figure 7 illustrates the LOS measurements from the ground observer to the RSO, with the true propagated inertial orbit overlaid with the propagated inertial orbit obtained kinematically from the IROD solution. The RMS angle residual between the propagated IROD solution and the LOS measurements, described in Equation (30), is 1.266×10^{-6} rad. This indicates that the IROD solution provides good agreement with the LOS measurements.

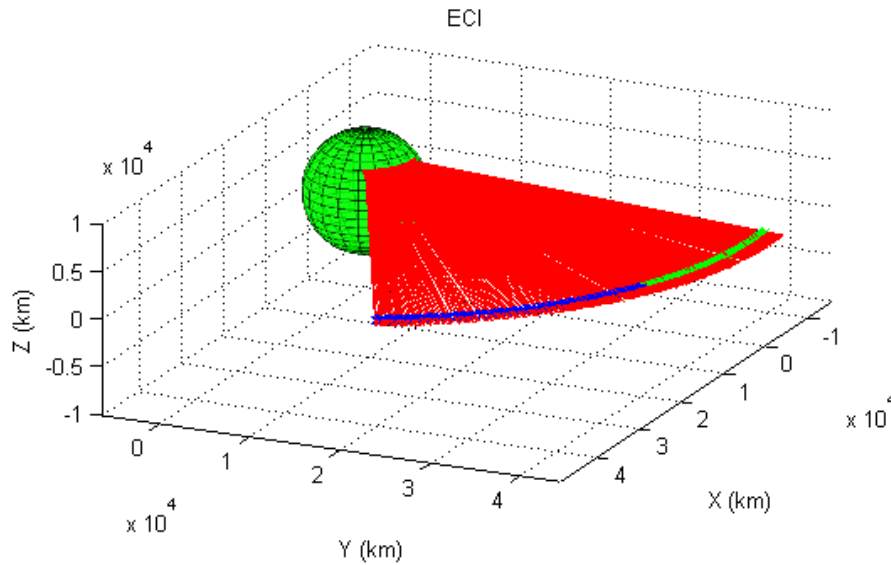


Figure 7. GIROD Scenario 1, with Observed Lines of Sight From Ground Sensor, Superimposed with True Propagated Trajectory (Blue) and IROD Solution Trajectory (Green)

The orbital elements for this solution are shown in Table 3, row (b). Because the IROD method requires a reference orbit in close proximity, it is instructive to use this IROD solution to define a new reference orbit and reapply the IROD method. This was performed in this particular case, with the resulting orbital elements shown in Table 3, row (c). The RMS angle residual is now 9.73×10^{-7} rad, indicating a slightly better agreement between this solution and the measurements than was obtained with the first IROD solution. Finally, Table 3, row (d) shows the true orbital elements of this scenario.

Table 3. Orbital Elements from Scenario 2 for (a) Constructed Reference Orbit, (b) First IROD Solution, (c) Second IROD Solution, (d) True Orbit

	a (km)	e	I (deg)	Omega (deg)	omega (deg)	perigee crossing time (SPM)
(a)	42,241.00	0	0.32343	296.299	undefined	undefined
(b)	42,552.15	0.001123	0.32773	326.917	326.501	4545.271
I	42,552.70	0.001137	0.32784	326.951	327.149	5095.156
(d)	42,551.78	0.001170	0.32782	327.031	326.220	4875.806

4.1.2 GIROD Scenario 2

Table 4. Description of GIROD Scenario 2, Including Table 1 Parameter Values

Dynamics order	Observer	Observed object	Reference object/orbit	# of measurements	Time span
1 st (NOM)	ground sensor	RSO	virtual	121	38pprox.. 2hrs

Next, Scenario 1 is rerun using a reduced measurement set. Only the first half of the measurements is used. The orbital elements from the resulting IROD solution are shown in Table 6. The values can be compared with the results in Table 3, and show good performance even in the presence of the smaller data set. The RMS angle residual is 6.73×10^{-7} rad.

Table 5. Orbital Elements from Scenario 2

a (km)	e	I (deg)	Omega (deg)	omega (deg)	perigee crossing time (SPM)
42,549.23	0.001148	0.32770	326.837	324.373	4396.959

4.1.3 GIROD Scenario 3

**Table 6. Description of GIROD Scenario 3, Including Table 1
Parameter Values**

Dynamics order	Observer	Observed object	Reference object/orbit	# of measurements	Time span
1 st (NOM)	ground sensor	RSO	virtual	60	39pprox.. 1hr

Finally, the same scenario is rerun using only the first quarter of the measurements. The orbital elements from the resulting IROD solution are shown in Table 8. Comparing these results to the values in Table 3, this reduced data set shows significant degradation in performance. But the solution can still be seen as a reasonable approximation of the true orbit. The RMS angle residual is 6.96×10^{-7} rad.

Table 7. Orbital Elements from Scenario 3

a (km)	e	I (deg)	Omega (deg)	omega (deg)	perigee crossing time (SPM)
42,566.07	0.001127	0.32713	326.851	339.372	8026.940

4.1.4 Assessment of GIROD Results

The NOM method has been utilized here as a novel way to perform ground-based IOD. With this method, the user is free to construct the reference orbit in any practical way. In most of the scenarios, NOM IROD solutions compare well to the simulated (2-body) truth trajectory. Note that the LMM and MRM methods are not applicable in the GIROD context, since both assume a space-based observer, whose orbit serves as the basis for the reference orbit.

4.2 CIROD

In these scenarios, the true RSO orbit from Table 3, row (d) is again used, and an observer satellite orbit is simulated so as to create a particular relative orbit between the observer and RSO. If the orbit element differences between the observer and RSO are small, in relative (LVLH) space the resulting motion is approximately a 2x1 ellipse in the x-y (radial/along-track) plane whose center is along the y axis, superposed with sinusoidal motion in the z (cross-track) direction. In each scenario, the true relative orbit will be expressed in terms of the relative orbit elements (ROEs) described in Subsection 3.4.4. Again, to represent realistic scenarios, a small amount of Gaussian error was added to each LOS measurement and to the observer's orbit (i.e. navigation error).

4.2.1 CIROD Scenario 1

Table 8. Description of CIROD Scenario 1, including Table 1 parameter values

Dynamics order	Observer	Observed object	Reference object/orbit	# of measurements	Time span
2 nd (LMM)	observer satellite	RSO	observer satellite	40	25hrs, 24min

Table 9. True Relative Orbit of CIROD Scenarios 1-4, in Terms of ROE Values

$a_{e,true}$ (km)	$x_{d,true}$ (km)	$y_{d,true}$ (km)	$z_{max,true}$ (km)	β_{true} (rad)	γ_{true} (rad)
20	0	0	10	0	0

Table 8 gives a basic description of this case, and Table 9 shows the ROE values of the true relative orbit. The time span of measurements is quite long, beyond one orbit period. Here the LMM method described in Subsection 3.2.1 was applied, which utilizes the second-order relative motion solution of [13-15]. The resulting RMS residual angle error over the 40 measurements, described in Equation (30), is 1.483265×10^{-2} rad.

Figure 8 depicts the estimated relative trajectory in blue in the x-y (radial/along-track) plane, along with line-of-sight vectors in red from the observer (at the origin) to the observed object at each measurement time. The points along the estimated relative trajectory at each measurement time are marked "x." This allows a visual assessment of the residuals. For comparison, the true relative orbit is shown in green. Note in this case that the true relative orbit is extremely small compared to the IROD solution. Figure 9 depicts the estimated relative trajectory in terms of z (cross-track) motion vs time, with the true z motion overlaid. Again, the IROD solution is in blue and the true motion is in green. The scheme of line styles and colors used in

Figure 8 and Figure 9 will be used throughout the next several CIROD scenarios.

Table 10 shows the ROE ratios for this scenario, as described in Subsection 3.4.4. Note that $\frac{a_{e,est}}{a_{e,comp}}$ and $\frac{z_{max,est}}{z_{max,comp}}$ are nearly equal and both very close to 1. Based on the discussion in Subsection 3.4.4, this indicates that the IROD solution agrees well with the true orbit except for a slight error in the scale factor, i.e. the estimated relative orbit is slightly smaller than the true relative orbit. (The x_d ratio is not a good indicator in this scenario because the “true” x_d is zero.)

Table 10. RMS Residual Angle Error and ROE Ratios for CIROD Scenarios 1-8

Scenario #	RMS angle (rad)	$\frac{a_{e,est}}{a_{e,true}}$	$\frac{x_{d,est}}{x_{d,true}}$	$\frac{z_{max,est}}{z_{max,true}}$
1	0.003806	0.872607	-0.07745	0.920783
2	0.00256	2.896092	-0.06374	3.128704
3	0.00905	0.824447	-1.4802	0.891407
4	0.000279	2.329194	-1.35423	2.983688

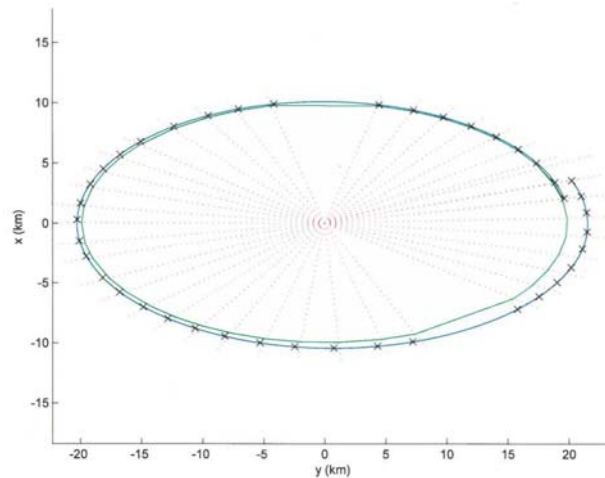


Figure 8. LVLH Trajectory of IROD Solution for CIROD Scenario 1 (x vs. y), with LOS Measurements and True Relative Orbit Displayed

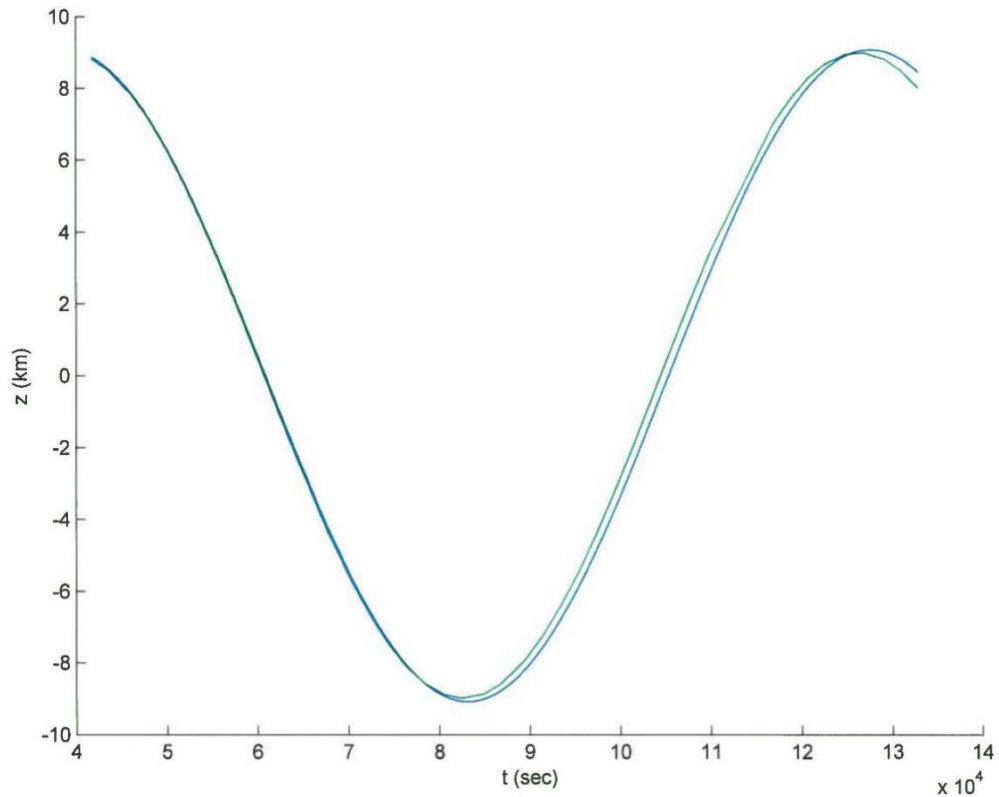


Figure 9. LVLH Trajectory of IROD Solution for CIROD Scenario 1 (z vs. t), with True Relative Orbit Displayed

4.2.2 CIROD Scenario 2

Table 11. Description of CIROD Scenario 2, Including Table 1 Parameter Values

Dynamics order	Observer	Observed object	Reference object/orbit	# of measurements	Time span
2 nd (LMM)	observer satellite	RSO	observer satellite	40	12hrs, 24min

Table 11 gives a basic description of this case. The true relative orbit is the same as that of Scenario 1, but the time span of measurements is approximately half that of Scenario 1. Here the LMM method was again applied, with a resulting RMS residual angle error of 2.560306×10^{-3} rad. Figure 10 depicts the estimated relative trajectory in the x-y plane, with line-of-sight vectors and the true relative orbit overlaid. Figure 11 depicts the estimated relative trajectory in terms of z (cross-track) motion vs time, with the true relative orbit overlaid. Table 10 shows the ROE

ratios for this scenario. Note that $\frac{a_{e,est}}{a_{e,comp}}$ and $\frac{z_{max,est}}{z_{max,comp}}$ are nearly equal, with both ratios approximately 3. Thus it can be concluded that the IROD solution in this scenario is somewhat less accurate than that for Scenario 1.

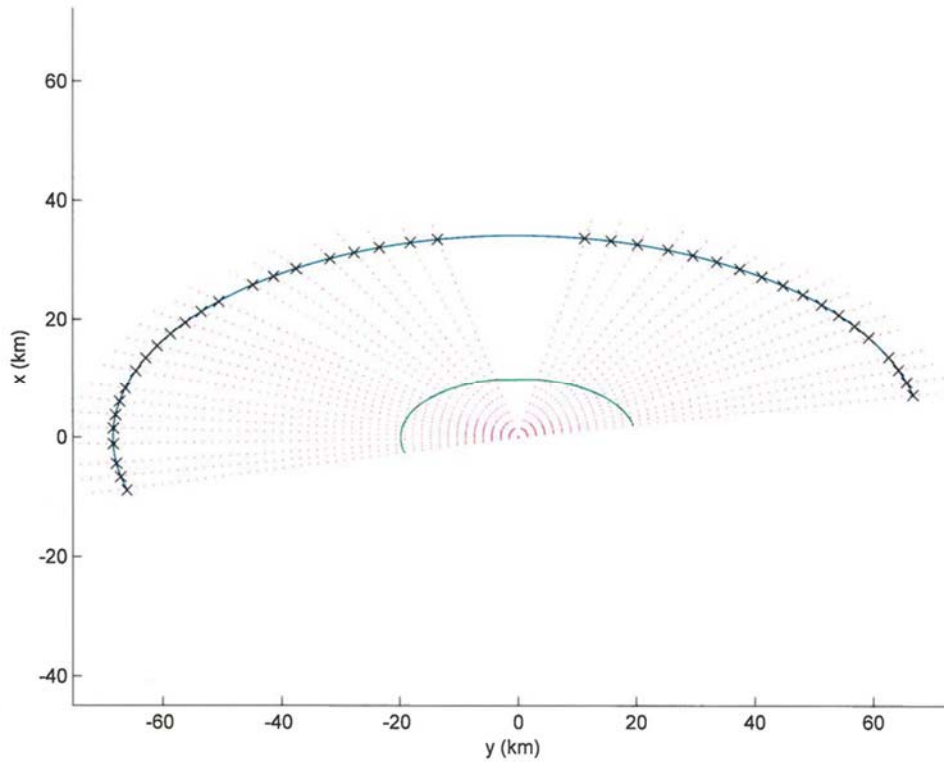


Figure 10. LVLH Trajectory of IROD Solution for CIROD Scenario 2 (x vs. y), with LOS Measurements and True Relative Orbit Displayed

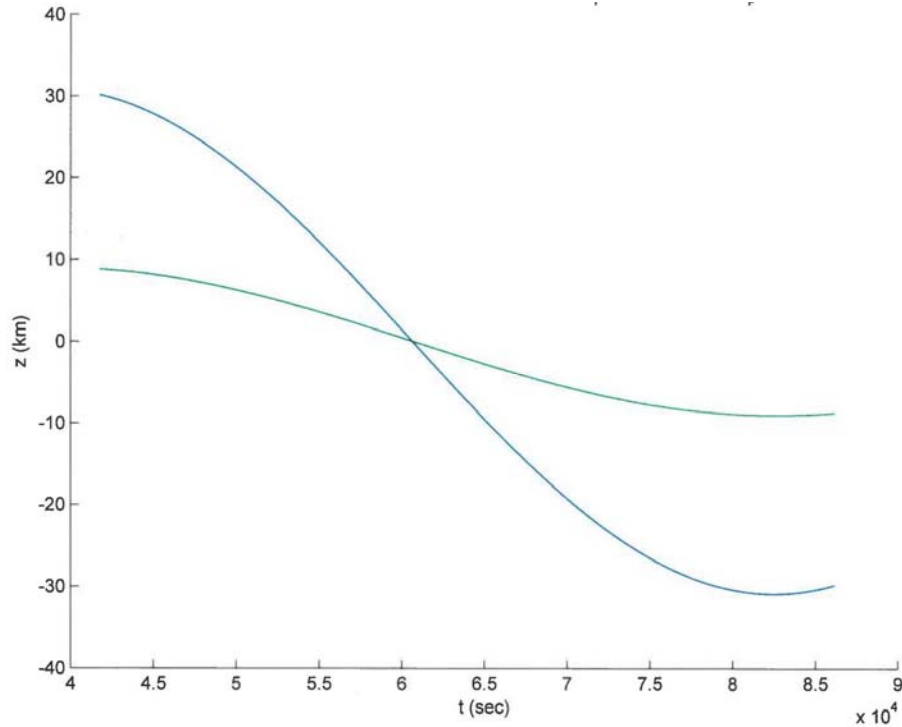


Figure 11. LVLH Trajectory of IROD Solution for CIROD Scenario 2 (z vs. t), with True Relative Orbit Displayed

4.2.3 CIROD Scenario 3

Table 12. Description of CIROD Scenario 3, Including Table 1 Parameter Values

Dynamics order	Observer	Observed object	Reference object/orbit	# of measurements	Time span
2 nd (LMM)	observer satellite	RSO	observer satellite	40	6hrs

Table 12 gives a basic description of this case. The true relative orbit is the same as that of Scenarios 1 and 2, but the time span of measurements is approximately half that of Scenario 2. Here the LMM method was again applied, with a resulting RMS residual angle error of 9.05196×10^{-3} rad. Figure 12 depicts the estimated relative trajectory in the x-y plane, with line-of-sight vectors and the true relative orbit overlaid. Table 10 shows the ROE ratios for this scenario. Judging from the ROE ratios, the IROD solution in this scenario is actually more accurate than that for Scenario 2, and nearly as accurate as that for Scenario 1.

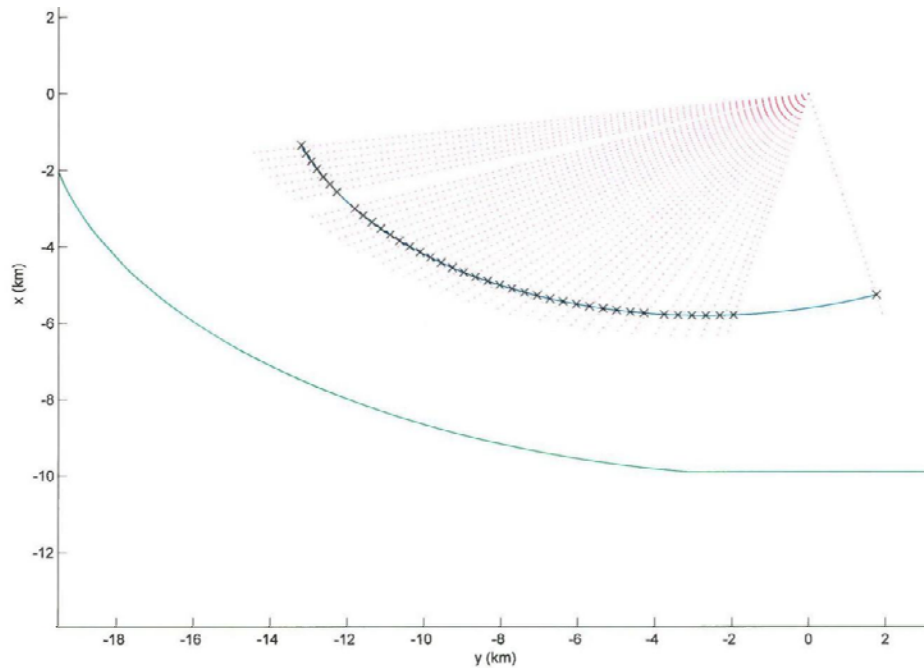


Figure 12. LVLH Trajectory of IROD Solution for CIROD Scenario 3 (x vs. y), with LOS Measurements and True Relative Orbit Displayed

4.2.4 CIROD Scenario 4

Table 13. Description of CIROD Scenario 4, Including Table 1 Parameter Values

Dynamics order	Observer	Observed object	Reference object/orbit	# of measurements	Time span
2 nd (LMM)	observer satellite	RSO	observer satellite	40	1hr

Table 13 gives a basic description of this case. The true relative orbit is the same as that of Scenarios 1-3, but the time span of measurements is reduced to one hour. Here the LMM method was again applied, with a resulting RMS residual angle error of 2.785607×10^{-4} rad. Figure 13 depicts the estimated relative trajectory in the x-y plane, with line-of-sight vectors and the true relative orbit overlaid. Table 10 shows the ROE ratios for this scenario. Judging from the ROE ratios, the accuracy of the IROD solution in this scenario is comparable to that of Scenario 2.

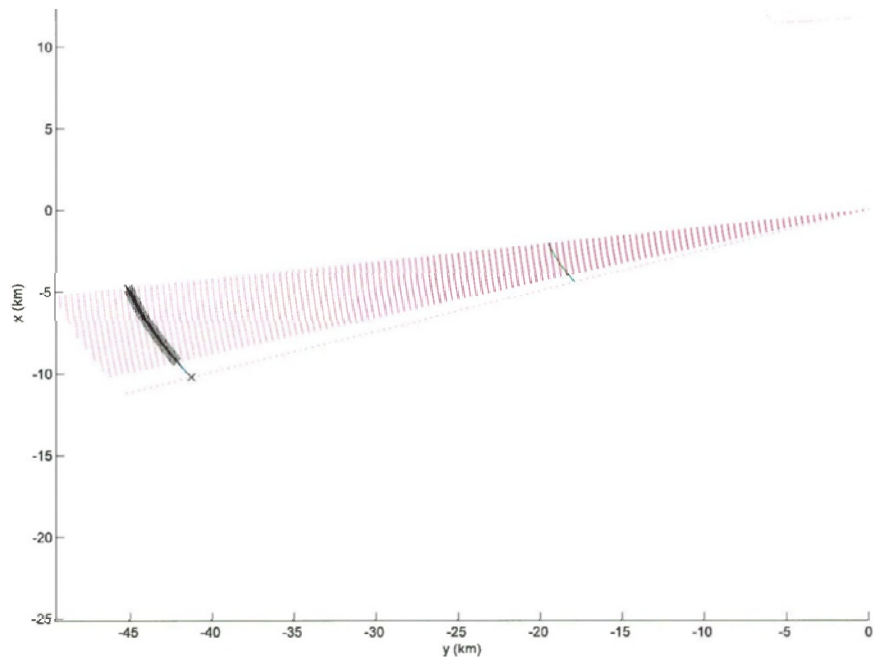


Figure 13. LVLH Trajectory of IROD Solution for CIROD Scenario 4 (x vs. y), with LOS Measurements and True Relative Orbit Displayed

4.2.5 CIROD Scenario 5

Table 14. Description of CIROD Scenario 5, Including Table 1 Parameter Values

Dynamics order	Observer	Observed object	Reference object/orbit	# of measurements	Time span
2 nd (MRM)	observer satellite	RSO	observer satellite	3	24hrs

Table 15. True Relative Orbit of CIROD Scenarios 5-6, in Terms of ROE Values

$a_{e,true}$ (km)	$x_{d,true}$ (km)	$y_{d,true}$ (km)	$z_{max,true}$ (km)	β_{true} (rad)	γ_{true} (rad)
12	1	30	5.5	0	0

The next two scenarios utilized the MRM method, which is constructed to solve a “square system,” i.e. 6 independent measurement equations in 6 unknown relative states. Therefore the number of LOS measurements processed for each of these scenarios will be 3. Table 14 gives a

basic description of this case, and Table 15 shows the ROE values of the true relative orbit. The time span of measurements is one orbit period.

The resulting RMS residual angle error over the 3 measurements processed is 6.656256×10^{-3} rad, while the RMS residual angle error over all available measurements during this time is 5.434810×10^{-3} rad.

Figure 14 depicts the estimated relative trajectory in the x-y plane, with line-of-sight vectors and the true relative orbit overlaid.

Figure 15 depicts the estimated relative trajectory in terms of z (cross-track) motion vs time, with the true relative orbit overlaid. Table 16 shows the ROE ratios and differences for this scenario. Specifically, ratios on a_e , x_d , y_d , and z_{max} are displayed, as well as differences in β at the initial

measurement time and γ . Note that $\frac{a_{e,est}}{a_{e,comp}}$, $\frac{x_{d,est}}{x_{d,comp}}$, $\frac{y_{d,est}}{y_{d,comp}}$, and $\frac{z_{max,est}}{z_{max,comp}}$ are all nearly equal, and

the γ and β differences are small. This indicates that the IROD solution agrees well with the true relative orbit except for a slight error in the scale factor.

Table 16. RMS Residual Angle Error and ROE Ratios/Differences for CIROD Scenarios 5-6

Scenario #	RMS angle (rad), 3 measurements	RMS angle (rad), all measurements	$\frac{a_{e,est}}{a_{e,comp}}$	$\frac{x_{d,est}}{x_{d,comp}}$	$\frac{y_{d,est}}{y_{d,comp}}$	$\beta_{est} - \beta_{comp}$ (rad)	$\frac{z_{max,est}}{z_{max,comp}}$	$\gamma_{est} - \gamma_{comp}$ (rad)
5	0.006656	0.005435	0.958401	0.589662	0.983845	0.056225	1.00872	-0.06497
6	0.000125	0.000102	2.777522	2.841772	4.40675	-0.00682	2.78567	0.008593

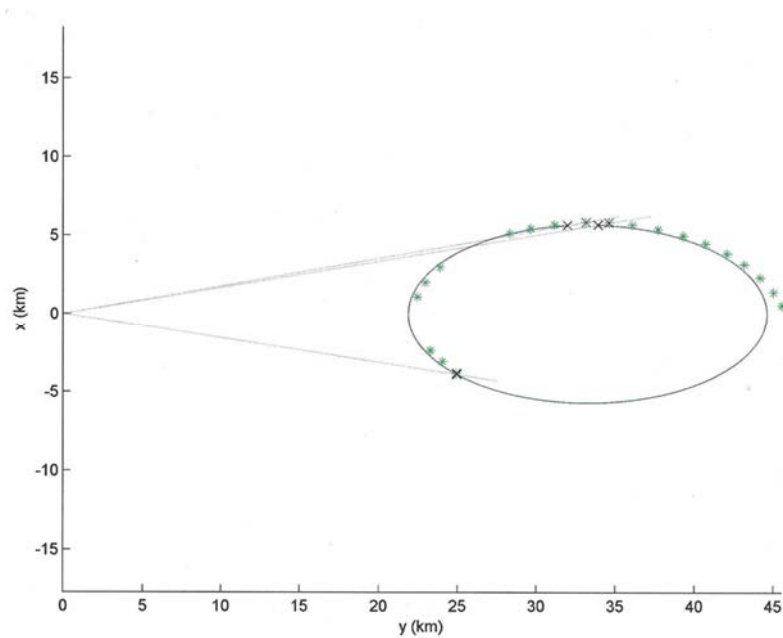


Figure 14. LVLH Trajectory of IROD Solution for CIROD Scenario 5 (x vs. y), with LOS Measurements and True Relative Orbit Displayed

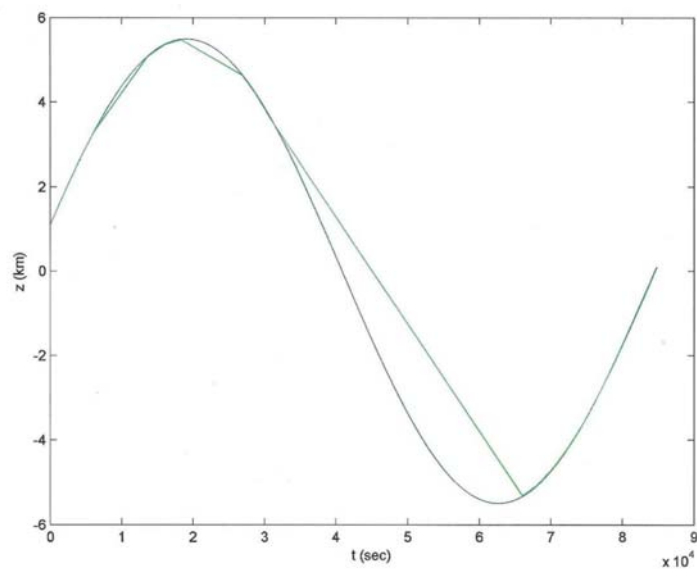


Figure 15. LVLH Trajectory of IROD Solution for CIROD Scenario 5 (z vs. t), with True Relative Orbit Displayed

4.2.6 CIROD Scenario 6

Table 17. Description of CIROD Scenario 6, Including Table 1 Parameter Values

Dynamics order	Observer	Observed object	Reference object/orbit	# of measurements	Time span
2 nd (MRM)	observer satellite	RSO	observer satellite	3	3hrs

Table 17 gives a basic description of this case. The true relative orbit is the same as that of Scenario 5, but the time span of measurements is reduced to 3hrs. Here the MRM method was again applied, with a resulting RMS residual angle error of 1.252948×10^{-4} rad over the 3 measurements processed, and 1.023028×10^{-4} rad over all available measurements.

Figure 16 depicts the estimated relative trajectory in the x-y plane, with line-of-sight vectors and the true relative orbit overlaid. Figure 17 depicts the estimated relative trajectory in terms of z (cross-track) motion vs time, with the true relative orbit overlaid. Table 16 shows the ROE ratios

and differences for this scenario. Here, $\frac{a_{e,est}}{a_{e,comp}}$, $\frac{x_{d,est}}{x_{d,comp}}$, $\frac{y_{d,est}}{y_{d,comp}}$, and $\frac{z_{max,est}}{z_{max,comp}}$ are roughly equal

but further from 1 than in Scenario 5, and again the γ and β differences are small. Thus it can be concluded that the IROD solution in this scenario is somewhat less accurate than that for Scenario 5.

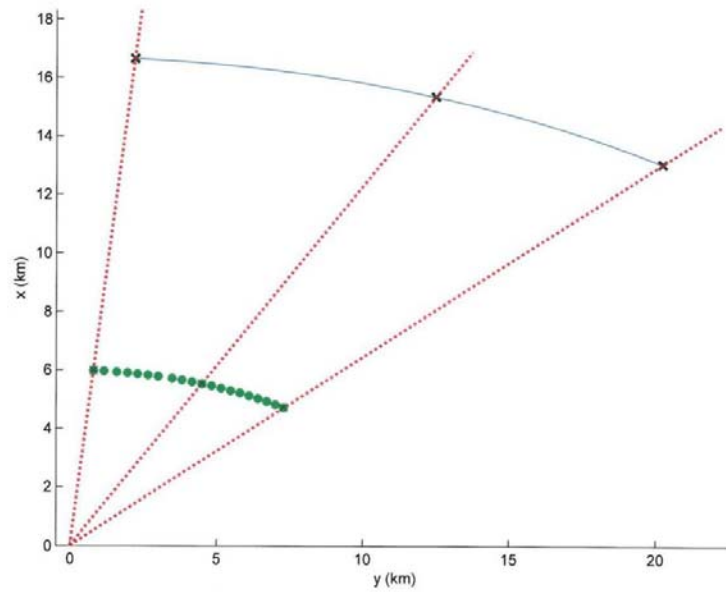


Figure 16. LVLH Trajectory of IROD Solution for CIROD Scenario 6 (x vs. y), with LOS Measurements and True Relative Orbit Displayed

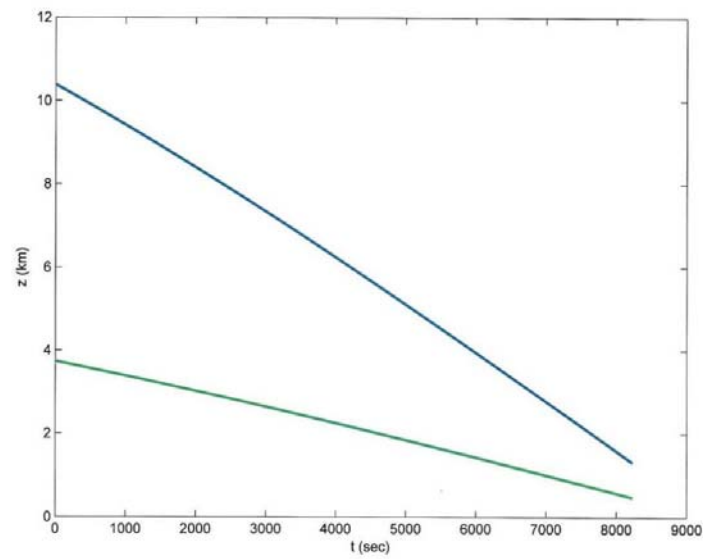


Figure 17. LVLH Trajectory of IROD Solution for CIROD Scenario 6 (z vs. t), with True Relative Orbit Displayed

4.2.7 CIROD Scenario 7

Table 18. Description of CIROD Scenario 7, Including Table 1 Parameter Values

Dynamics order	Observer	Observed object	Reference object/orbit	# of measurements	Time span
2 nd (MRM)	observer satellite	RSO	observer satellite	19	13hrs,30m

Table 19. True Relative Orbit of CIROD Scenarios 7-8 (Pre-maneuver), in Terms of ROE Values

$a_{e,true}$ (km)	$x_{d,true}$ (km)	$y_{d,true}$ (km)	$z_{max,true}$ (km)	β_{true} (rad)	γ_{true} (rad)
32	0	0	10	0	0

The next two scenarios utilized the NOM method, which takes advantage of maneuvering by the observer to enhance observability. As mentioned previously, the success of NOM depends on a significant enough maneuver to cause deviation in the observer's position from the reference orbit at each measurement time that is greater than deviation due simply to position error. Likewise, the change in post-maneuver LOS measurements, compared to the measurements had the vehicle not maneuvered, should be greater than LOS error.

Table 18 gives a basic description of this case, and Table 19 shows the ROE values of the true relative orbit at the initial time (i.e. before the observer maneuvers). The time span of measurements is just over one-half orbit period, and 19 measurements (sampled evenly across the entire set) were utilized for the solution.

The resulting RMS residual angle error over the 19 measurements processed is 1.924892×10^{-2} rad. Figure 18 depicts the estimated relative trajectory in the x-y plane, with line-of-sight vectors and the true relative orbit overlaid. The line-of-sight vectors are plotted in red at each measurement time, originating from the observer and pointing in the direction of the RSO. The deviation of the vehicle from the reference orbit (i.e. the origin of the plot) due to maneuvering is evident. A small amount of maneuvering begins within the first few measurement times, then a significant maneuver occurs between the 11th and 12th measurements, moving the vehicle roughly 15km downrange of the reference orbit by the 12th measurement time. It should be re-emphasized that the NOM method estimates the RSO's motion in the LVLH frame of the reference orbit. Since the reference orbit was constructed based on the observer's orbit at the first measurement time (call this t_0), the IROD trajectory depicted is the "pre-maneuver" orbit, i.e. the relative orbit the vehicle would see for all time had it remained on the orbit that it possessed at t_0 . The true relative trajectory is seen to match the LOS vectors early on, until maneuvering begins causing the vehicle to "see"

a different relative orbit. If the authors had kinematically converted the true relative orbit from the instantaneous LVLH frame of the observer to the “pre-maneuver” LVLH frame, the green asterisks would closely match the LOS vectors at every measurement time. Figure 19 depicts the estimated relative trajectory in terms of z (cross-track) motion vs time, with the true relative orbit overlaid. Here again the effect of vehicle maneuvering is evident, as the true relative orbit matches the IROD trajectory fairly closely at first, then begins to deviate slightly, and deviates more significantly later on. Table 20 shows the ROE ratios and differences for this scenario. Again, the a_e and z_{max} ratios are roughly equal, and are both near 1. This indicates that the IROD solution generally matches the true relative orbit, including the scale factor. (The x_d ratio is not a good indicator in this scenario because the “true” x_d is zero.)

Table 20. RMS Residual Angle Error and ROE Ratios/differences for CIROD Scenarios 7-8

Scenario #	RMS angle (rad)	$\frac{a_{e,est}}{a_{e,comp}}$	$\frac{x_{d,est}}{x_{d,comp}}$	$\beta_{est} - \beta_{comp}$ (rad)	$\frac{z_{max,est}}{z_{max,comp}}$	$\gamma_{est} - \gamma_{comp}$ (rad)
7	0.019249	0.845896	-59.6686	-0.06662	1.045267	0.063935
8	0.006483	1.842167	83.21633	-0.0419	1.77918	0.025322

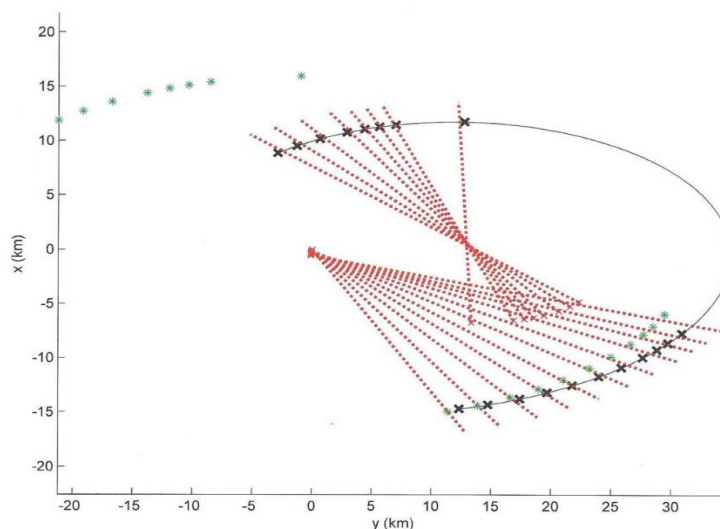


Figure 18. LVLH Trajectory of IROD Solution for CIROD Scenario 7 (x vs. y), with LOS Measurements and True Relative Orbit Displayed

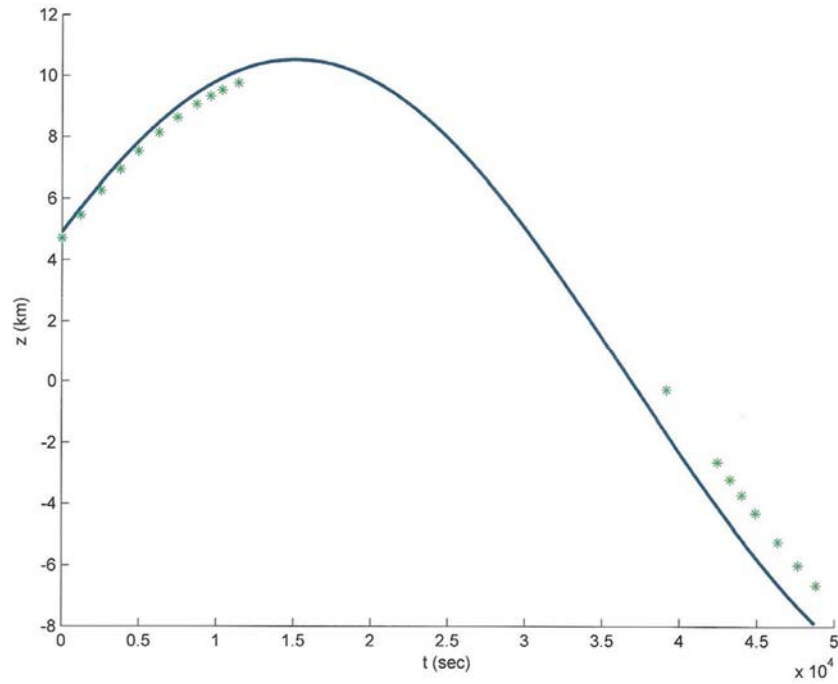


Figure 19. LVLH Trajectory of IROD Solution for CIROD Scenario 7 (z vs. t), with True Relative Orbit Displayed

4.2.8 CIROD Scenario 8

Table 21. Description of CIROD Scenario 8, Including Table 1 Parameter Values

Dynamics order	Observer	Observed object	Reference object/orbit	# of measurements	Time span
2 nd (MRM)	observer satellite	RSO	observer satellite	8	2hrs,25m

This scenario is initialized with the same conditions as the previous scenario, but the time span of measurements is reduced to roughly 2.5 hours. Table 21 gives a basic description of this case. Here the NOM method was again applied, with a resulting RMS residual angle error of 6.483021×10^{-3} rad. Figure 20 depicts the estimated relative trajectory in the x-y plane, with line-of-sight vectors and the true relative orbit overlaid. As mentioned in the previous scenario, only a small amount of maneuvering occurs during this span of measurements. This accounts for the true relative orbit matching the LOS vectors early on, then deviating slightly. Figure 21 depicts the estimated relative trajectory in terms of z (cross-track) motion vs time, with the true relative orbit overlaid. Table 20 shows the ROE ratios for this scenario. These ratios reflect a scale factor error of approximately 2. The fact that that this IROD solution does not compare as well with the true relative orbit as the solution of Scenario 7 makes logical sense, since the amount of maneuvering by the observer during the span of measurements was much less than in Scenario 7.

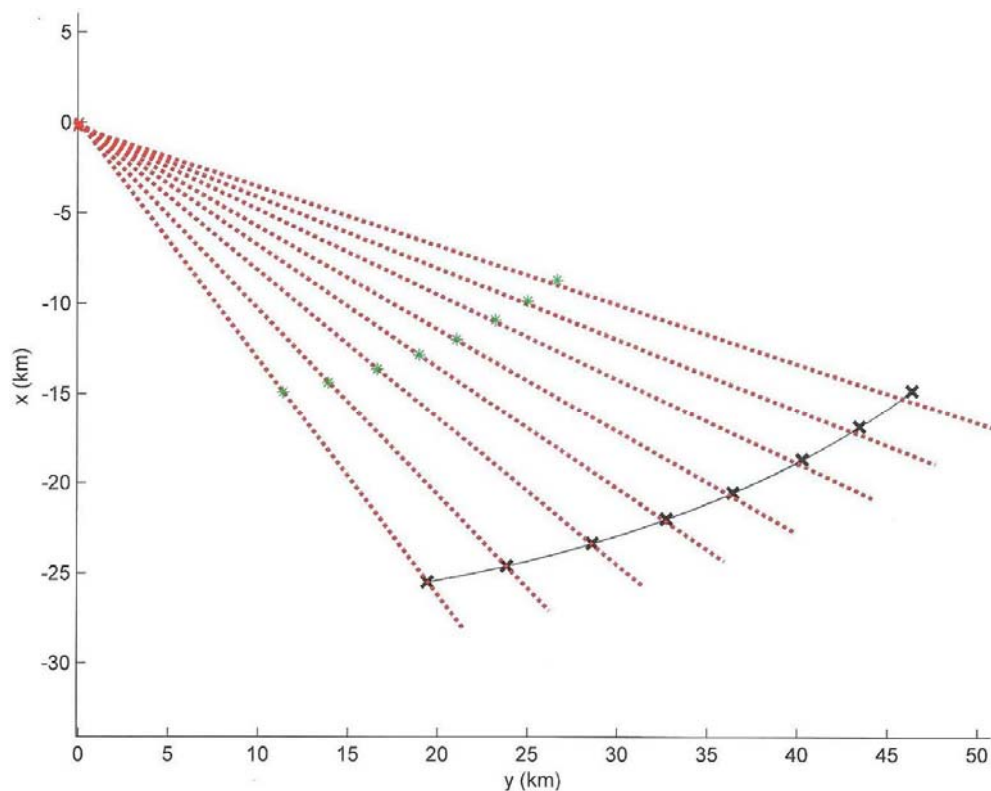


Figure 20. LVLH Trajectory of IROD Solution for CIROD Scenario 8 (x vs. y), with LOS Measurements and True Relative Orbit Displayed

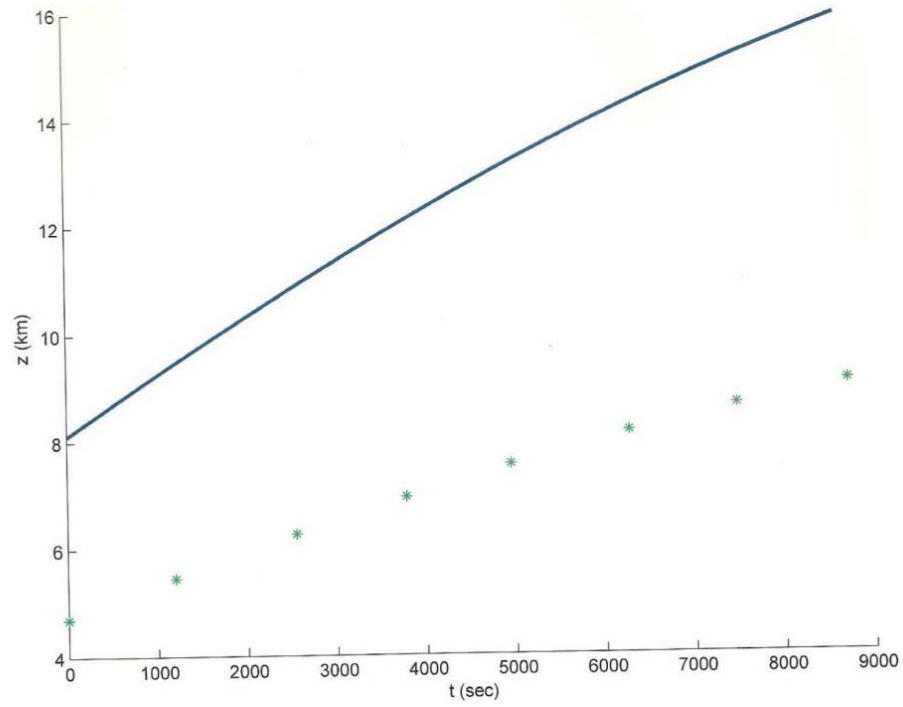


Figure 21. LVLH Trajectory of IROD Solution for CIROD Scenario 8 (z vs. t), with True Relative Orbit Displayed

5 CONCLUSIONS

This report has detailed a relative motion-based approach to angles-only initial orbit determination known as IROD and introduced multiple techniques applied in several scenarios pertinent to both classical (ground-based) orbit determination scenarios and close-proximity navigation missions. Each technique is based on “relaxation” of one of the conditions known to guarantee observability, a phenomenon that would lead to an infinite number of ambiguous solutions. The techniques are as follows:

- Linear Matrix Method (LMM): relies on second-order relative orbit dynamics to avoid observability; processes any number of line-of-sight measurements, utilizing singular-value decomposition to yield a least-squares solution
- Matrix Resultant Method (MRM): a linear-algebra-based approach that also utilizes second-order relative orbit dynamics; constructed to find a trajectory that exactly fits three line-of-sight measurements
- Nonhomogeneous Observer Method (NOM): utilizes linear relative orbit dynamics and assumes that the observer does not lie on the reference orbit during all the measurement times; processes any number of measurements, yielding a least-squares solution via matrix pseudoinverse

These techniques require *no* knowledge of the observed object, other than the line-of-sight measurements to the object. Unlike most classical initial orbit determination methods (and precise orbit determination methods for that matter), the IROD methods require no iteration or recursion; the only method requiring any “decision making” is MRM, which tends to yield multiple solutions that must be disambiguated. In most cases, the disambiguation process is straightforward and can be implemented algorithmically.

The IROD methods were tested in two categories of scenarios: ground-based observations of an RSO and close-proximity observations from a space-based observer to the RSO. Results were not compared with other means of initial orbit determination, but rather with simulated “true” relative orbits. In most of the cases displayed, the IROD solution compared well with the true relative orbit. The performance of the methods seems to be sensitive to the following factors:

- *Knowledge of the observer’s location at each measurement time*
- *Spatial separation between the reference orbit and the observed object’s orbit*: For NOM, this should be as small as possible; for LMM and MRM, this should be large enough for nonlinear effects to induce observability, but not so large that the second-order model does not accurately represent the motion
- *Temporal separation between the first and last measurement time*: This should be long enough that enough change in the motion occurs to induce observability, but not so long that the dynamic model employed incurs significant propagation error
- *Line-of-sight measurement error*

For the results displayed, the most common error exhibited by the solutions was a “scale factor” error, whereby the estimated orbit matches “truth” in terms of shape, phase, etc, but over- or under-estimates the magnitude of the motion. Based on the discussion early in the report, this is expected in close-proximity scenarios, where the motion is quasi-linear. However, in many of the example scenarios it appears the scale factor is just as likely due to measurement error than quasi-linearity. A goal of future work is to better understand this correlation, as described below. At any rate, the capability of these techniques to approximate scale factor fairly well is a significant step beyond how a method based solely on linear homogeneous dynamics (e.g. Clohessy-Wiltshire) would perform. Any method of the latter variety has no means whatsoever to approximate scale factor, due to “Woffinden’s dilemma,” which leads to a solution consisting of an infinite family of trajectories rather than a specific one.

For some categories of scenarios explored, not all three IROD methods were applicable, i.e. ground-based observation scenarios, only NOM could be used because the observer was on the ground and not in orbit. For close-proximity scenarios where the observer maneuvered, only NOM was applied, whereas in close-proximity scenarios where the observer did not maneuver, only LMM and MRM were applied. This illustrates a sensitivity factor additional to those listed above: degree of “observer non-homogeneity” in the scenario. In other words, NOM requires *non-homogeneous* observer motion in order to be successful, but LMM and MRM require *homogeneous* observer motion in order to be successful. This implies that there may exist some threshold of “observer non-homogeneity” that serves as the minimum for NOM to be successful and simultaneously the maximum for LMM and MRM to be successful. A goal of future work described below is to develop a hybrid of these methods that utilizes both the nonlinear effects required by LMM and MRM and the non-homogeneous effects required by NOM. Such a method would likely perform well regardless of how much or little degree of “observer non-homogeneity” exists.

This report demonstrates that with further development, *all three IROD methods have potential to be effective initial orbit determination tools*. The fact that they do not require iteration or other “human in the loop” intervention makes them attractive candidates for autonomous operation, either on-board a spacecraft or on the ground in situations where time and resources for “inspection” of solutions is scarce. In addition to these specialized scenarios, the methods may prove effective for more general use if they compare well to classical initial orbit determination techniques. A future effort will be to survey all angles-only initial orbit determination techniques past and present, and characterize them in terms of such aspects as complexity, speed, accuracy, and robustness to error. It will then be evaluated how well the three IROD methods compare to these existing methods in the above respects, using a variety of simulated and real test scenarios.

6 RECOMMENDATIONS

Other planned future work includes:

- Further testing in each of the above categories of scenarios, as well as other scenarios (e.g. Low Earth Orbit (LEO) to Geosynchronous Orbit (GEO) scenarios, choosing an Space-based Space Surveillance (SBSS-like observer)
- Characterize the correlation between measurement error and scale factor in IROD solutions
- Develop a hybrid IROD technique that exploits both second-order relative orbit dynamics and non-homogeneous observer motion
- Derive expressions for IROD solution covariance, based on measurement error covariance
- Test the viability of IROD solutions by injecting them into precise orbit determination schemes (e.g. various strains of Kalman filters)
- Explore statistical initial orbit determination techniques (e.g. Constrained Admissible Region) in order to (1) compare Monte Carlo runs of the IROD methods to a single Constrained Admissible Region solution, and (2) possibly develop a relative motion-based version of the Constrained Admissible Region philosophy
- Combine the IROD capability with an image processing capability (e.g. the software package Geodetica) to directly convert images of space objects into orbit solutions

REFERENCES

1. Chory, M. A., Hoffman, D. P., Lemay, J. L.; "Satellite Autonomous Navigation – Status and History," *PLANS '86 – Position Location and Navigation Symposium*, Las Vegas, NV, Nov. 1986.
2. Schutz, B. E., Tapley, B. D., Born, G. H.; *Statistical Orbit Determination*, Elsevier Academic Press, 2004.
3. Evans, J. W.; Piñon, E., Mulder, T. A.; "Autonomous Rendezvous Guidance and Navigation for Orbital Express and Beyond," *2006 AAS/AIAA Space Flight Mechanics Meeting*, Tampa, Florida, 25 January 2006.
4. Rumford, T. E.; "Demonstration of Autonomous Rendezvous Technology (DART) Project Summary," *Proc. SPIE 5088, Space Systems Technology and Operations*, 10 (August 6, 2003); doi:10.1117/12.498811, 2003.
5. Mitchell, I. T., Gorton, T. B., Taskov, K., Drews, M. E., Luckey, R. D., Osborne, M. L., Page, L. A., Norris, H. L., and Shepperd, S. W.; "GN&C Development of the XSS-11 Micro-Satellite for Autonomous Rendezvous and Proximity Operations," *29th Annual AAS Guidance and Control Conference*, Breckenridge, CO, 2006.
6. G. H. Stokes, C. V. Braun, R. Sridharan, D. Harrison, and J. Sharma; "The Space-Based Visible Program," *Lincoln Laboratory Journal*, Vol. 11, No. 2, pp. 205–238, 1998.
7. Fujimoto, K. and Scheeres, D. J.; "Short-Arc Correlation and Initial Orbit Determination for Space-Based Observations," *2011 AMOS Conference*, Maui, HI, 2011.
8. Woffinden, D.; *Angles-Only Navigation for Autonomous Orbital Rendezvous*. PhD thesis, Utah State University, Logan, Utah, Aug. 2008, <http://digitalcommons.usu.edu/etd/12>.
9. Curtis, H.; *Orbital Mechanics for Engineering Students*, Elsevier Academic Press, 2013.
10. Escobal, P., *Methods of Orbit Determination*, John Wiley & Sons, 1965.
11. Tschauner, J. F. A. and Hempel, P. R.; "Rendezvous zu einem in elliptischer Bahn umlaufenden Ziel," *Astronautica Acta*, Vol. 11, No. 2, pp. 104–109, 1965.
12. Clohessy, W. H. and Wiltshire, R. S.; "Terminal Guidance System for Satellite Navigation," *Journal of Aerospace Sciences* 29, pp. 653–658, 1960.
13. London, H. S.; "Second Approximation to the Solution of the Rendezvous Equations," *AIAA Journal*, Vol. 1, No. 7, pp. 1691–1693, 1963.
14. Anthony, M. L. and Sasaki, F. T.; "Rendezvous Problem for Nearly Circular Orbits," *AIAA Journal*, Vol. 3, No. 7, pp. 1666–1673, 1965.
15. Newman, B. A. and Lovell, T. A.; "Second Order Nonlinear Boundary Value Solution for Relative Motion Using Volterra Theory," *AAS Paper 13-470, presented at the AAS/AIAA Space Flight Mechanics Meeting*, Kauai, HI, Feb 10-14, 2013.
16. Macaulay, F. S.; *The Algebraic Theory of Modular Systems*, Cambridge University Press, 1916.

17. LeGrand, K., DeMars, K., and Darling, J.; "Solutions of multivariate polynomial systems using Macaulay resultant expressions," *AAS/AIAA Space Flight Mechanics Meeting*, Santa Fe, New Mexico, Jan 2014.
18. Garg, S.K. and Sinclair, A.J.; "Initial Relative-Orbit Determination Using Second-Order Dynamics and Line-of-Sight Measurements," *AAS 15-390, AAS/AIAA Space Flight Mechanics Meeting*, Williamsburg, Virginia, 11-15 January 2015.
19. Kirwan, F.; *Complex Algebraic Curves*, Cambridge University Press, Cambridge, England, 1992.
20. Schaub, H. and Junkins, J.; "*Analytical Mechanics of Space Systems*," AIAA, Reston, VA, 2009.
21. Lovell, T.A. and Tragesser, S.G.; "Guidance for Relative Motion of Low Earth Orbit Spacecraft Based on Relative Orbit Elements," *AAS/AIAA Astrodynamics Specialist Conference*, Providence, RI, Aug 16-19, 2004.
22. Lovell, T.A. and Spencer, D.A.; "Relative Orbital Elements Formulation Based upon the Clohessy-Wiltshire Equations," *Journal of the Astronautical Sciences*, Volume 61, Issue 4, pp. 341-366, Dec 2014.

LIST OF SYMBOLS, ABBREVIATIONS, AND ACRONYMS

Az/El	Azimuth/elevation
CIROD	Close-Proximity IROD
ECI	Earth-Centered Inertial
GEO	Geosynchronous Orbit
GIROD	Ground-based IROD
GPS	Global Positioning System
IOD	Initial Orbit Determination
IROD	Initial Relative Orbit Determination
LEO	Low Earth Orbit
LMM	Linear Matrix Method
LOS	Line-of-sight
LVLH	Local-Vertical-Local-Horizontal
MRM	Matrix Resultant Method
NOM	Nonhomogeneous Observer Method
PI	Principal Investigators
RA/Dec	Right ascension/declination
ROE	Relative Orbit Element
RMS	Root Mean Square
RSO	Resident Space Object
SBSS	Space-based Space Surveillance
SRP	Solar Radiation Pressure
TLE	Two-line Element

DISTRIBUTION LIST

DTIC/OCP

8725 John J. Kingman Rd, Suite 0944
Ft Belvoir, VA 22060-6218

1 cy

AFRL/RVIL

Kirtland AFB, NM 87117-5776

2 cys

Official Record Copy

AFRL/RVSV/Thomas A. Lovell

1 cy